UNIVERSITY OF OKLAHOMA

GRADUATE COLLEGE

OUTCROP-SCALE STUDY OF THE PERMIAN BONE SPRING FORMATION, BONE SPRING CANYON, GUADALUPE MOUNTAINS, TEXAS: FRACTURE CHARACTERIZATION

A THESIS

SUBMITTED TO THE GRADUATE FACULTY

in partial fulfillment of the requirements for the

Degree of

MASTER OF SCIENCE

By

ABDULLAH ABDULJALIL ALABBAD
Norman, Oklahoma
2017

OUTCROP-SCALE STUDY OF THE PERMIAN BONE SPRING FORMATION, BONE SPRING CANYON, GUADALUPE MOUNTAINS, TEXAS: FRACTURE CHARACTERIZATION

A THESIS APPROVED FOR THE
CONOCOPHILLIPS SCHOOL OF GEOLOGY AND GEOPHYSICS

BY

_____
Dr. John D. Pigott, Chair

_____
Dr. Kurt Marfurt

_____
Dr. Kulwadee L. Pigott

Acknowledgements

I thank Allah first and last for granting me the health and will to complete this project. Several people have provided me with help and guidance, without whom the completion of this project could not have been possible. I would like to start by thanking my advisor Dr. John D. Pigott for sharing his knowledge in science with me and as well as for being supportive and a good friend. Without the help and support from Dr. Pigott, the completion of this project would not be possible. I would like as well to thank my committee members, Dr. Kurt Marfurt, and Dr. Kulwadee Pigott, for their guidance and support.

I would like to thank Keith MacPherson for sharing his knowledge with me and for providing me with continuous support. I would also to thank the family of the exploration and technical services unit at Saudi Aramco for being supporting and accommodating.

I would also like to thank the Dr. Jonena Hearst from the Guadalupe National Park Services for helping me get a permit to conduct my research in the park. I would also like to thank Brian Norton for providing continuous support on how to use Split-Fx software.

I would like to give special thanks to the following graduate students for helping me out throughout the data acquisition phase and for their enjoyable comrade: Andreas Hernan Ruiz Lozano, Emma Giddens, Kathryn Garrett, Zhuobo Wang, Daniel Sigward, Andrew Brown, John Hornbuckle, Fadel Al Hussain, and Hussain Al Saleh.

Finally, I would like to thank my father Abduljalil AlAbbad, my mother Worod Al-Hussain, and my wife Kouther AlAbbad for their continuous support and for being patient.

Dedicated to the blessed souls of Abduljalil Jumah Alarbash, Mohammed Hassan Al-binessa, Mohammed Jumah Alarbash, and Hadi Salman Alhashim for sacrificing their lives in a heroic effort that stopped an ISIS bomber reaching a mosque. A verse in the Holy Qura'an states: ***"He who saves a life it's as if he saved all mankind, he who kills a life it's as if he killed all mankind."*** May Allah bless their souls and grant their families strength and patience

Table of Contents

List of Tables

List of Figures

Abstract

A light detection and ranging- (LiDAR) focused outcrop study was conducted on Upper Leonardian Bone Spring limestone in the Bone Canyon, Delaware Basin of West Texas. LiDAR technology is very useful in modeling fracture systems from outcrop data. It provides several advantages such as accessibility to regions where hand measurements are not possible, a greater density of data, and a convenient PC-powered platform for interpretation. Using LiDAR data, a population of 7449 fracture planes was delineated and characterized. Fracture planes represented 3 major sets: E-W trending Fracture Set-1, N-S trending Fracture Set-2, and NE-SW trending Fracture Set-3. Fracture sets were used to delineate stress fields within the Bone Canyon. Fracture Set-1 is more systematic (containing closely spaced fractures and is characterized with uniform strikes) and older corresponding to a N-S sigma 3. Fracture Set-2 and Set-3 is less systematic (containing variably spaced fractures and is characterized with less uniform strike) and are younger corresponding to present day stress field that corresponds to a general E-W and NW-SE sigma 3, respectively.

Statistics of fractures planes across rock units on the north and south canyon walls showed some variations indicating that parameters such as bed thickness and bedding pattern (whether a rock unit is thinly or thickly bedded) can influence the distribution of fractures, their density, and intensity. The north wall has an average fracture density of 2.6 fractures/m^2 while the south wall has an average fracture density of 1.23 fracture/m^2.

Chapter 1 Introduction

The Permian Basin of West Texas and New Mexico has been a target for scientific investigations since the 1850's when G. G. Shumard took the initiative to collect Permian fossils that were interpreted to represent the base of El Capitan formation. The continued interest in the Permian Basin was not only to provide an understanding for the geology of the region, but also to determine the economic potential of this region. The Permian Basin has been recognized as a major hydrocarbon producing region in North America since oil was first discovered in 1920's (Keller et al., 1980). Despite the massive efforts that have been made to unravel the geologic history of the basin, there are still many areas where further investigations are needed (Crosby, 2015). This research aims to shed light on the Delaware Basin; a sub-basin of the Permian Basin. The primary reason for this investigation is to provide possible insight into understanding the fracture relationships of the Upper Bone Spring from an outcrop study which may impact unconventional exploration of the Bone Springs in the subsurface.

In recent years, the Permian Basin in Texas and New Mexico has come to prominence to become the top oil producing area in the United States exceeding the federal offshore Gulf of Mexico region. As of 2013, the Permian Basin's contribution to the total U.S. crude oil production was around 18% (EIA, 2014). Between 2007 to 2013, oil production from the Permian Basin increased from 850,000 barrels per day (bbl/d) to 1,350,000 (bbl/d) scoring a 60% increase in production. This increase was mainly driven by the contribution of six formations within the Permian Basin that include Delaware, Glorieta, Yeso, Bone Spring, Wolfcamp, and Spraberry (EIA, 2014).

Three of these formations (Wolfcamp, Bone Spring, and Spraberry formations) alone contributed to about 75% of the increase in the Permian Basin crude oil production. Between 2007 to 2013, production from these three formations increased from 140,000 (bbl/d) to 600,000 (bbl/d). Their contribution was not only limited to increasing the production from the Permian Basin, but also spurred other economic benefits such as driving an increasing rig activity especially in horizontal, oil-directed drilling activity (EIA, 2014). The 2015 EIA's annual report "U.S. Crude Oil and Natural Gas Proved Reserves, 2014" highlighted that the Permian Basin's reserve additions to the Texas crude oil and lease condensate proved reserves additions was around 50% of total additions. These additions by the Permian Basin also accounted for one-third of the net proven reserves addition for the entire United States for 2014. Bone Spring and Wolfcamp plays of New Mexico and Texas together added 387 MMBbl of proved reserves between 2013 and 2014 (EIA, 2015).

The Bone Spring play on the western margin of the greater Permian Basin (see Figure 1.1) is, as highlighted previously, a major play and a great contributor within the Permian Basin. Oil production was initially limited to the permeable section of the Bone Spring. However, advanced technologies such as horizontal drilling and hydraulic fracturing allowed for commercial production from the Bone Spring formation's low permeability sections (EIA, 2014).

Natural fractures as well are an important element to study within the Bone Spring Formation. Natural fractures can be an instrumental tool in providing high initial production rates. In addition, open fractures can result in enhanced permeability within a target reservoir (Dutton et al., 2004). Apparently, fractures are an important

element of the Bone Spring Formation and a systematic and detailed fracture characterization study is needed. The advent of advanced technologies such as Light Detection and Ranging (LiDAR) allow imaging fracture complexes at a very high resolution. This study will introduce a scheme and provide analysis for fracture complexes within the exposed walls of the Bone Spring formation inside the Bone Canyon located in the north-western margins of the Delaware Basin.

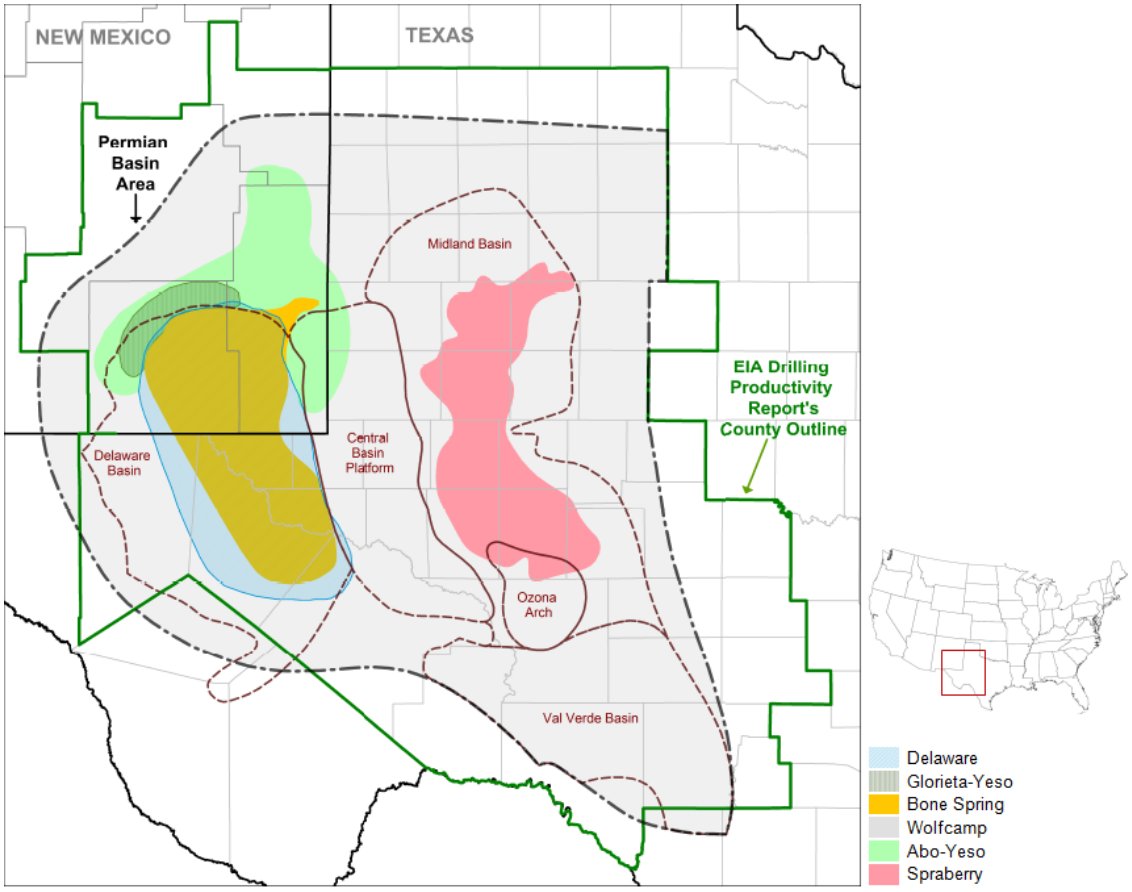

Figure 1.1 Map of the major oil-and-gas-producing formations in the Permian Basin. The Bone Spring play is highlighted in gold/yellow color and is located on the western margin of the Permian Basin. Adapted from EIA (2014).

Study Location

Figure 1.2 highlights the location of the study area, denoted by the red star on the (left) image, on the northwestern margin of the Delaware Basin within the greater Permian Basin of West Texas and Southeast New Mexico. Outcrops of the Bone Spring are located within the Bone Canyon along the west-facing escarpment of the mountains as highlighted in Figure 1.2. The Bone Canyon's type locality is approximately 1-2 miles northwest of the El Capitan peak (King, 1948). The Bone Canyon generally trends east-west exhibiting north-south facing characteristic exposures of the Bone Spring Formation.

The yellow circle in Figure 1.2 highlights a total of 10 scanning positions within the canyon. LiDAR scan positions were selected based on several criteria such as geology of the region and accessibility.

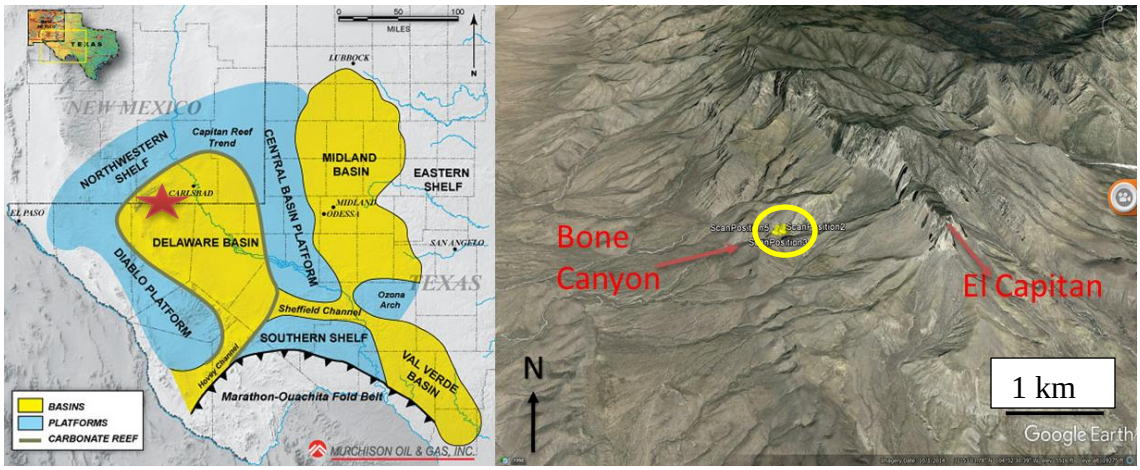

Figure 1.2. Map of the major geologic provinces within the Permian Basin (left); Adapted from Marathon Oil & Gas INC. A Google Earth Image (right) showing the study area and other key geologic features.

Problem Definition

The Leonardian Bone Spring Formation within the Delaware Basin's subsurface consists of three major units, from top to base; the Upper Bone Spring Sand (1st), the Middle Bone Spring Sand (2nd), and the Lower Bone Spring Sand (3rd). According to Montgomery (1997), fractures within the Upper and Lower Bone Spring Formation sand layers, the producing zones within the Delaware Basin fields, have greatly contributed to the production capabilities of the field by enhancing porosity and permeability. A clear understanding of fracture complexes within the Bone Spring Formation is clearly of a great importance. Therefore, this study will investigate the different types of fractures within the Upper Bone Spring Formation using LiDAR in Bone Spring Canyon and in so doing an attempt to provide some aspects to its tectonic history and possible insight into optimizing its exploration.

Chapter 2 Geological Background

The Delaware Basin occupies the westernmost part of the Permian Basin. Figure 2.1. highlights a general stratigraphic column of the Delaware Basin, and a detailed section of the Leonardian Bone Spring formation bounded by the Guadalupian Brushy Canyon from the top and the Wolfcampian succession at its base. The Delaware Basin is around 200 miles long and 100 miles wide. It occupies a structural depression resting against the eastern face of the Front Range. The Delaware Basin is known for hosting a wide range of tectonic and sedimentary features (Adams, 1965). The Delaware Basin is bounded to the west by the Diablo Platform, Northwestern Shelf to the northwest, Capitan Reef Trend to the northeast, Central Basin Platform to the east, and the Marathon-Ouachita Fold Belt to the south (see Figure 1.2 and Figure 2.2). The Delaware Basin is also affected by the Hovey Channel which connects the Delaware Basin to the Panthalassia Ocean to the south and the Sheffield Channel to the southeast which is a connection to the Midland and Val Verde neighboring basins (Crosby, 2015).

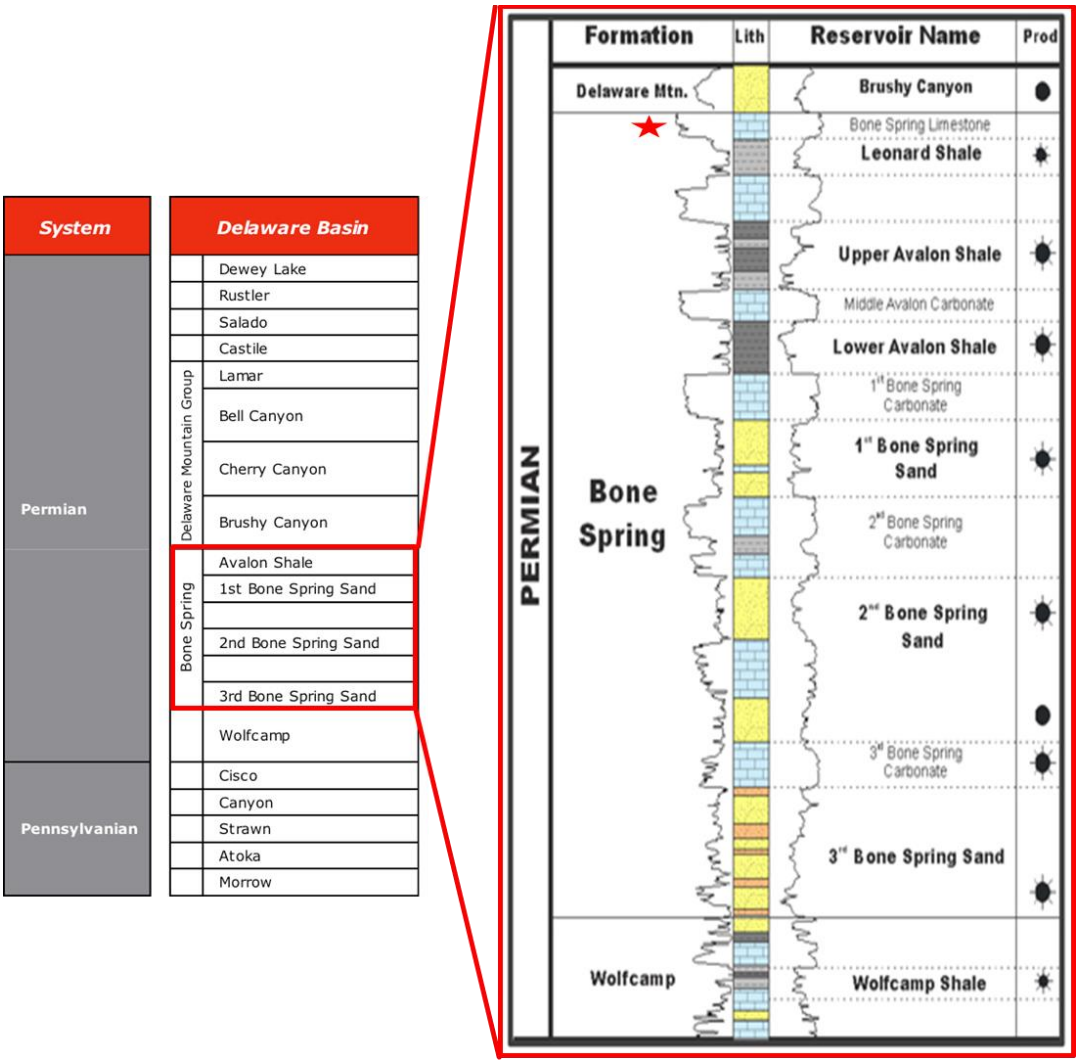

Figure 2.1 General stratigraphic column of the Delaware Basin. A more detailed section of the Bone Spring Formation is presented as well (right). The red star to the right denotes a tentative stratigraphic position for the outcrops exposed in the study area (King, 1948). The detailed Bone Spring section highlights the major reservoirs within the Bone Spring Formation. (Adapted and modified from Murchison Oil and Gas, 2014, and Crosby, 2015)

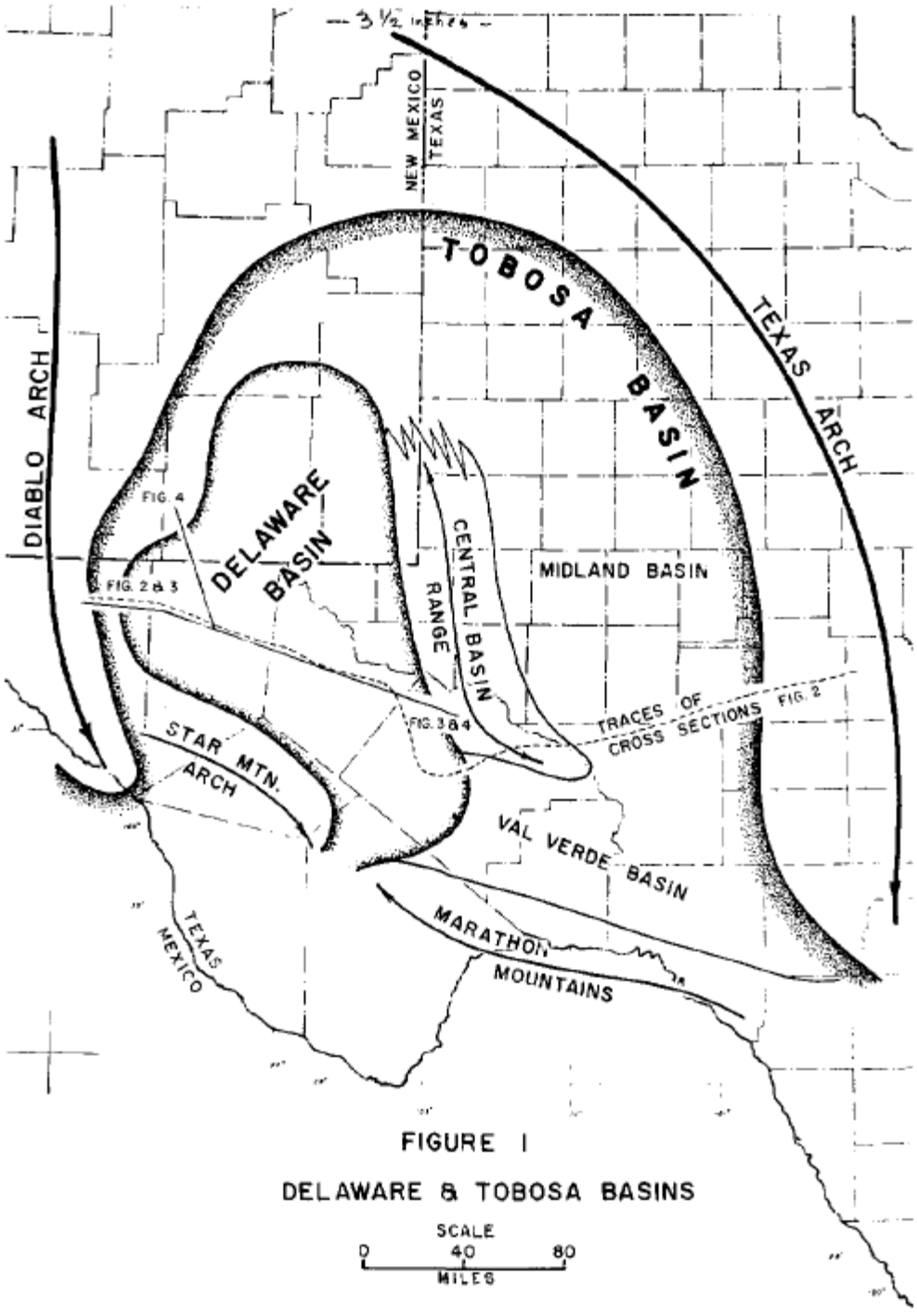

Figure 2.2. Delaware and Tobosa Basins. This figure highlights major features surrounding the Delaware Basin. (Adapted from Adams, 1965)

Stratigraphy

The Leonardian Bone Spring Formation within the Delaware Basin consists of three major units: the Upper Bone Spring Sand (1st), the Middle Bone Spring Sand (2nd), and the Lower Bone Spring Sand (3rd). The Bone Spring Formation has formed under a mixed carbonate-siliciclastic system reflecting sea level fluctuations during the Leonardian with carbonates depositing during high sea levels and sandstones depositing during low sea levels. Carbonate layers within the Bone Spring are characterized by the presence of interbedded strata of carbonaceous shaly siltstones, and a muddy lithology ranging from mudstone to wackstone (Montgomery, 1997). In addition, dolopackstones, with open fractures, were encountered within the Mescalero Escarpe reservoir. The open fractures resulted in enhanced permeability within the reservoir. Carbonate debris of the Bone Spring tend to flow from the central basin to the northeastern sub-basin. These flows are localized near the toe of slope of the Abo and Yeso shelf edge (Dutton et al., 2004). The Bone Spring sand strata represent submarine fan deposits and are mainly composed of carbon rich, calcareous interbeds of shale and siltstone (Montgomery, 1997). In addition, siliciclastic turbidites, consisting of fine-grained sandstones with dolomite and authigenic clay cement, are abundant within the three Bone Spring Sand units (Gawloski, 1988).

Tectonic Evolution

The early history of the formation of the Delaware Basin began as early as the late Precambrian and Cambrian when the transcontinental arch was spurred off by a peninsular to extend southeastward across the southeastern parts of modern day New Mexico and neighboring western Texas (Adams, 1965). This tectonic evolution continued to develop and involved a conversion of the crest of the peninsular ridge into an axis of a negative basin. The leading cause for this negative depression may have been the response of the underlying crust and mantle rocks to episodes of cooling and shrinking (Adams, 1965). Subsidence continued to proceed slowly until a structural basin was produced. However, subsidence did not only produce a structural basin, but also produced a flattened coastal plain that was flooded by Early Ordovician transgression (Adams, 1965). This Early Ordovician northwestward-transgression resulted in depositing the oil- and gas-rich Ellenburger reservoir layers. The Middle Ordovician resembled an important phase in the development of the Delaware Basin as it marked the development of its ancestral basin; the Tobosa Basin. The Tobosa Basin formed as a 350-mile-wide sag between the Texas arch on the east and Diablo arch on the west. The lower parts of the Tobosa Basin were primarily filled with sandstone, limestone, and shale coming from the highlands north of the Tobosa Basin sag (Adams, 1965). During the Upper Ordovician, Silurian, and Devonian, axial areas of the basin corresponding to deep water. Due to various factors such as increasing water acidity and/or lack of nutrients, deposition of limestone was limited in the basin. This resulted in increasing subsidence rate and decreasing sedimentation rate. In addition, central parts of the basin started to expand shoreward. The most important highlight of this

period is the creation of more accommodation space in the started central parts of the basin that were later filled with Mississippian deposits (Adams, 1965). Prior to the Mississippian, a slight uplift affected the sediment-starved central basinal parts and exposed the Silurian-Devonian-and- Upper Ordovician shelf deposits. The Mississippian began by a transgression that filled the sediment-starved parts of the basin with the Woodford Shale (Adams, 1965). The key event that initiated the formation of the Delaware Basin was the compressional stress that started to develop during the Late Mississippian affecting the ancestral Tobosa Basin. These stresses, over time, started to form a median ridge that split the Tobosa Basin into two sub-basins; the Midland and Delaware basins (Adams, 1965). During the early Pennsylvanian, the Delaware Basin was rapidly subsiding. During both Early and Late Pennsylvanian, the Delaware Basin was starved and only thin layers were deposited (Adams, 1965). The Lower Permian is characterized by accumulation of thick turbidite sequences in the Delaware basin. This was accompanied by rapid subsidence rates that caused high rates of compressional stresses in the underlying crustal stresses. Compressional stresses resulted in uplifting the median fault-block range that separated between the Delaware and Midland basins. A new arch was formed on the southwestern side of the Delaware Basin called the Star Mountain arch to denote the Early Permian structural spur that extends southeastward from the Diablo arch. A series of uplifts followed and hindered the compressional stresses.

Subsidence continued during the Mid-Permian (Leonardian), the period of Bone Spring Formation deposition. During Leonardian, basinal deposits consisted mainly of dark limestone, shale, and fine-grained sandstone with a significant presence of chert

(Adams, 1965). During this time, limestone shelves developed toward the Diablo arch toward the west. Poorly-pronounced barrier reefs protected those shelves especially on shallow north margins. Channels started to develop through the reefs and started supplying the basin with clastic sediment influx. In addition, alluvial fans started to form in front of the channels. The introduction of this clastic influx allowed for the forestepping reefs and contributed to the growth of the seaward shelf. The Upper Permian was controlled by reef growth rather than tectonism. The rate of reef growth created lithological differences between rocks of the Guadeloupian and Ochoan. The Upper Permian was tectonically stable; its thick layers were mainly a result of filling the depression that was created in previous Permian epochs (Adams, 1965).

Petroleum Exploration History

Interest in the Lenonardian Bone Spring formation of the Delaware basin was low in the last two decades of the 20th century, resulting in few publications on the Bone Spring formation in the Delaware basin. In addition, the low interest has caused a lack of documentation about some drilling targets that have taken place. During the early exploration and production phase, carbonate and clastic slope deposits were the main exploration targets. However, basinal areas have proven to be more prolific in recent years (Hart, 1997).

Production and exploration trends have been varying over the years depending on oil prices. Within the Delaware Basin, Bone Spring fields had nominal depths of around 8,000-10,000 ft. Because of the varying, mostly dropping, oil prices and the great depths, the Bone Spring formation in last two decades of the 20th century was regarded as a secondary target (Hart, 1997).

In recent years, the Bone Spring play has become a main target. The major development in the play has occurred because of the considerable advancements in horizontal drilling and fracturing. The Bone Spring play is classified as a gas-condensate play based on its liquid yield. Commercially, the Bone Spring play is rated as the most attractive play among the tight oil plays within the Permian basin with an estimated $49 BOE break-even price for the top five operators (Berman, 2016). This rate is considered low when compared to the whole Permian Basin tight oil plays averaged break-even price of $61 BOE (Berman, 2016). The chart in Figure 2.3 provides information about three of the major Permian Basin tight oil plays for top operators.

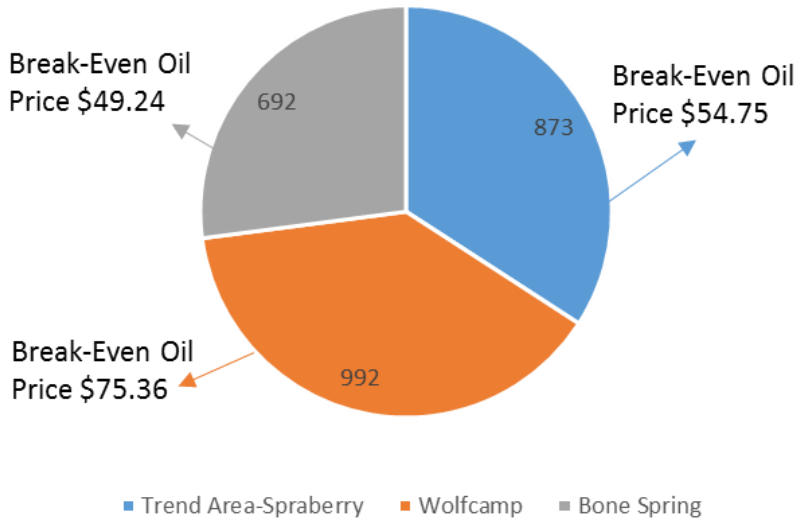

Figure 2.3. Number of wells and weighted average break-even price in selected Permian basin tight oil plays for top operators. (Modified from Berman, 2016)

The Bone Spring play is attractive not only due to having the low break-even oil price of $49, but also due to having high EURs (estimated ultimate recovery) calculated from decline-curve analysis. For this decline curve, the average Bone Spring well EUR, based on production data from 5 operators, is approximately 294,000 BOE. Figure 2.4 and Figure 2.5 highlight the type decline curve for Bone Spring wells and the estimated ultimate production for Bone Spring wells, respectively. A map of the Bone Spring play commercial areas was created based on two cut-off values: $45 and $60 Figure 2.6.

This map highlights the great potential of the Bone Spring play when prices go higher than the break-even oil price (Berman, 2016).

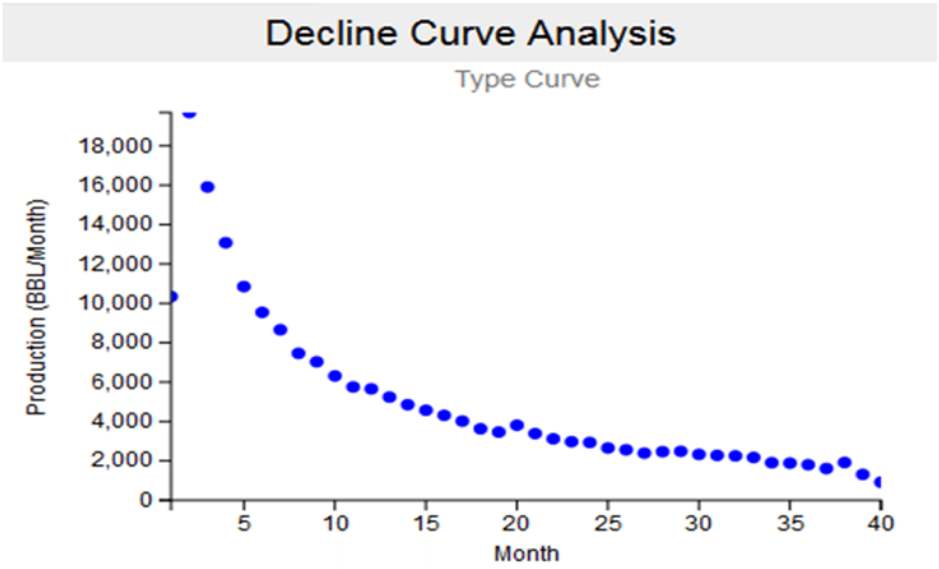

Figure 2.4 Type decline curve for Delaware Basin Bone Spring wells that have a minimum production of 100,000 BO, (Nibbelink, 2016)

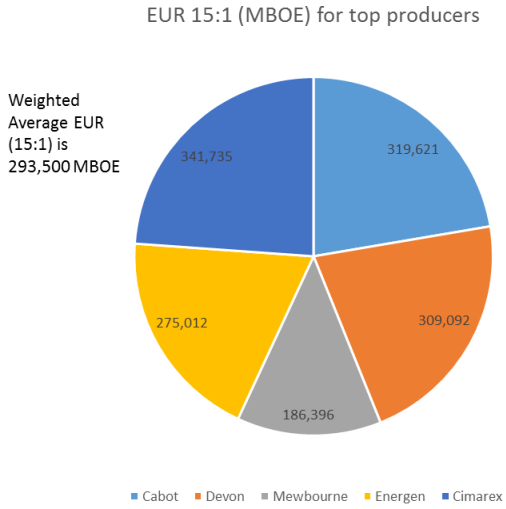

Figure 2.5 EUR (estimated ultimate recovery) 15:1 from decline curve analysis for the main operators in the Bone Spring Play. (Modified after Berman, 2016)

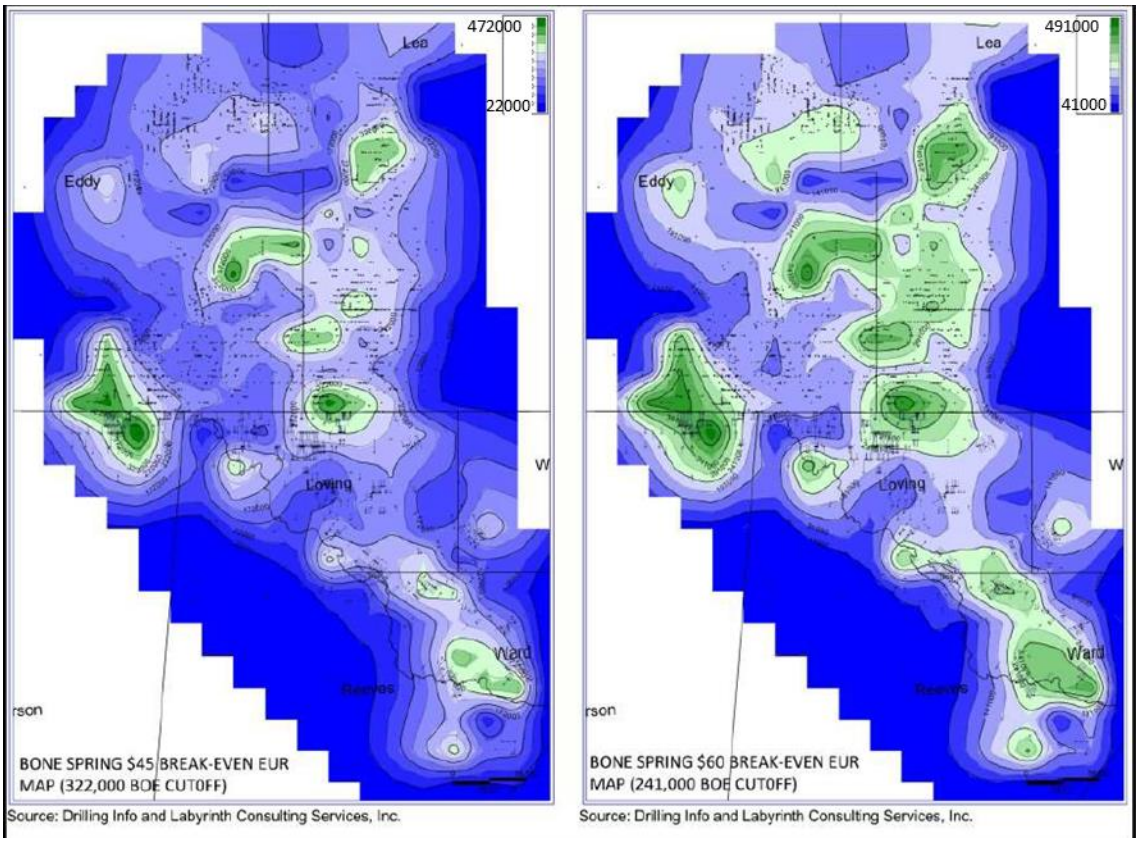

Figure 2.6 Commercial area maps for the Bone Spring play at two break-even prices: $45 (left), and $60 (right) BOE. (Modified after Berman, 2016)

Chapter 3 Methods

The advent of advanced technologies such as Light Detection and Ranging (LiDAR) allow imaging fracture complexes at a very high resolution. In addition, LiDAR enables accessing and studying areas that were inaccessible before using hand measurements. A RIEGL VZ-400 3D terrestrial laser scanner was utilized to scan outcrops of the Bone Spring formation within the Bone Canyon. It provides remote data acquisition using a narrow infrared laser beam. Table 3-1 provides range performance data for a RIEGL VZ-400 scanner.

Table 3-1 RIEGL VZ-400 Scanner's Range Performance. Adapted from http://www.riegl.com/uploads/tx_pxpriegldownloads/10_DataSheet_VZ-400_2014-09-19.pdf

Performance Range	Long Range Mode	High Speed Mode
Pulse repetition rate PRR (peak)	100 kHz	300 kHz
Effective Measurement Rate	42,000 measurements/sec	122,000 measurements/sec
Max. Measurement Range		
natural targets ρ ≥ 90%	600 m	350 m
natural targets ρ ≥ 20%	280 m	160 m
Max. Number of Targets per Pulse	practically unlimited	
Accuracy	5 mm	
Precision	3 mm	

LiDAR Procedure

Geological reconnaissance was the first step in achieving the goal of this study. It allowed the determination of scanning location, and the proper preparation for the acquisition phase. Reconnaissance was first started in the office by going through literature and using satellite images from Google Earth to select proper candidate scanning locations. The second phase of reconnaissance involved visiting the site, determining the exact scanning positions and acquiring GPS measurements for the selected scanning positions. When selecting the final scanning position, a surveyor needs to take into consideration the ability to access the location and the careful selection of a scanning position that will result in minimum shadow zones. Shadow zones are areas on the scanned target that yield no reflectivity. In this study, most shadow zones resulted because of the morphology of the scanned walls that force the emitted laser beam to run parallel to some areas (Hanzel, 2014). When the emitted laser beam runs parallel to a surface, the reflected energy is equal to zero. The applicable solution to compensate for shadow zones is taking multiple scans of the same target from different angles.

Data Acquisition

In order to successfully acquire data that is valid for interpretation, various tools are also utilized in the data acquisition. A Nikon D-800 was attached to the VZ-400 scanner in order to take panoramic views of the canyon. At each scan position, seven photos were taken to provide a panoramic view for the scanned object. These pictures were later used to color the point cloud data acquired by the scanner. Other equipment used included an HP laptop, a scanner tripod, power cables, a scanner battery, a car battery, cylinder reflectors, and flat reflectors.

Once the scanning position is finalized and the LiDAR is mounted to the tripod, the reflectors are then placed in various locations along the target. When making multiple scans, a minimum of three reflectors is needed to stitch the scans together (RIEGL, 2013). The acquisition phase included 10 scanning positions. Panoramic scans were acquired at each position with a resolution of 0.20-0.25 degrees. The mode for scanning was set to Long Range (ideal for large objects and long distance). The GPS unit attached to the LiDAR was set to accurate position estimation mode. This mode enables the GPS unit to provide more accurate positioning for the LiDAR machine by communicating with the nearest satellite. The GPS attached to the LiDAR is more accurate than the commercial GPS units available in the market (Hanzel, 2014). For each scan position, the scanning time was around 70-80 minutes from equipment setup to moving to the next scan position.

A VZ-400 scanner can be wired or connected wirelessly to a laptop. Data are acquired in the form of point cloud (x, y, z). Point clouds of each scan can be internally stored in the LiDAR or instantaneously transferred to the laptop. Using RiScan (a point

cloud acquisition and processing application), a surveyor manually selects the reflectors and determines their type. A fine scan is later done in order to better identify the reflectors and register them as tie-points that can be used to stitch scans together. After fine-scanning in each scan position, each two consecutive scans are tied together using a minimum of three reflectors. After tying the scans, the surveyor can disassemble the equipment and move to another scan position.

Processing

Data processing was done on two processing platforms: RiScan Pro and Split-FX. RiScan Pro was mainly utilized to condition the acquired data and prepare it for fracture characterization. Split-FX was mainly utilized for fracture characterization using automated and/or user-manipulated interpretations of point cloud data imported from RiScan Pro.

RiScan Pro

RiScan Pro is an acquisition and processing platform for handling data in point cloud format. Point cloud data are stored in X, Y, Z format where X, and Y usually express lateral changes and Z denotes vertical changes. Handling data in point cloud format allows one to combine multiple scans into one composite scan. The data can be processed and displayed as either amplitude or reflectance data. Amplitude is used to describe the echo signal received by the scanner and is dependent of several factors such as the aperture of the receiver, the angle and range of the target, and the laser pulse intensity. Amplitude value is a ratio that correlates the amplitude of the detected echo signal and the amplitude of the echo signal at the detection threshold of the scanner (RIEGL, 2013). Reflectance is different as it doesn't depend on the angle and range. Reflectance compares the actual amplitude of the target to the amplitude of a reference flat white target within the same rage. Both reflectance and amplitude are measured in decibels (dB) (RIEGL, 2013). The major processing techniques involved running a multi-station adjustment in case there was a separation in the point cloud data, running some filters (such as Octree and Terrain filters) to clean-up the data, and coloring the scans. After making sure there is no separation in the data, images taken using Nikon

D800 are processed to eliminate any blurriness and distortion by using a ready-installed function in RiScan Pro. The undistorted images are later used to color the scans by creating a color spectrum and tying it with either reflectance or amplitude data. Some filters can be applied to further condition the data such as the octree filter and the terrain filter. Octree filter conditions the data by removing or merging point cloud data based on a cubic structure (RIEGL, 2013). The cube later is subdivided into smaller cubes of equal size until a size threshold is reached. The Octree filter provides the advantage of thinning heavily clustered zones without losing resolution (RIEGL, 2013). The terrain filter is used to remove vegetation from point cloud. This is done by comparing the reflection from vegetation with the reflection of the neighboring rock mass. Vegetation tends to bear higher reflectance values than the neighboring rock mass. After coloring, filtering, and cleaning up the data, the point cloud data from selected windows are exported in XYZ ASCII file format to be processed in Split-FX engineering software (Hanzel, 2014).

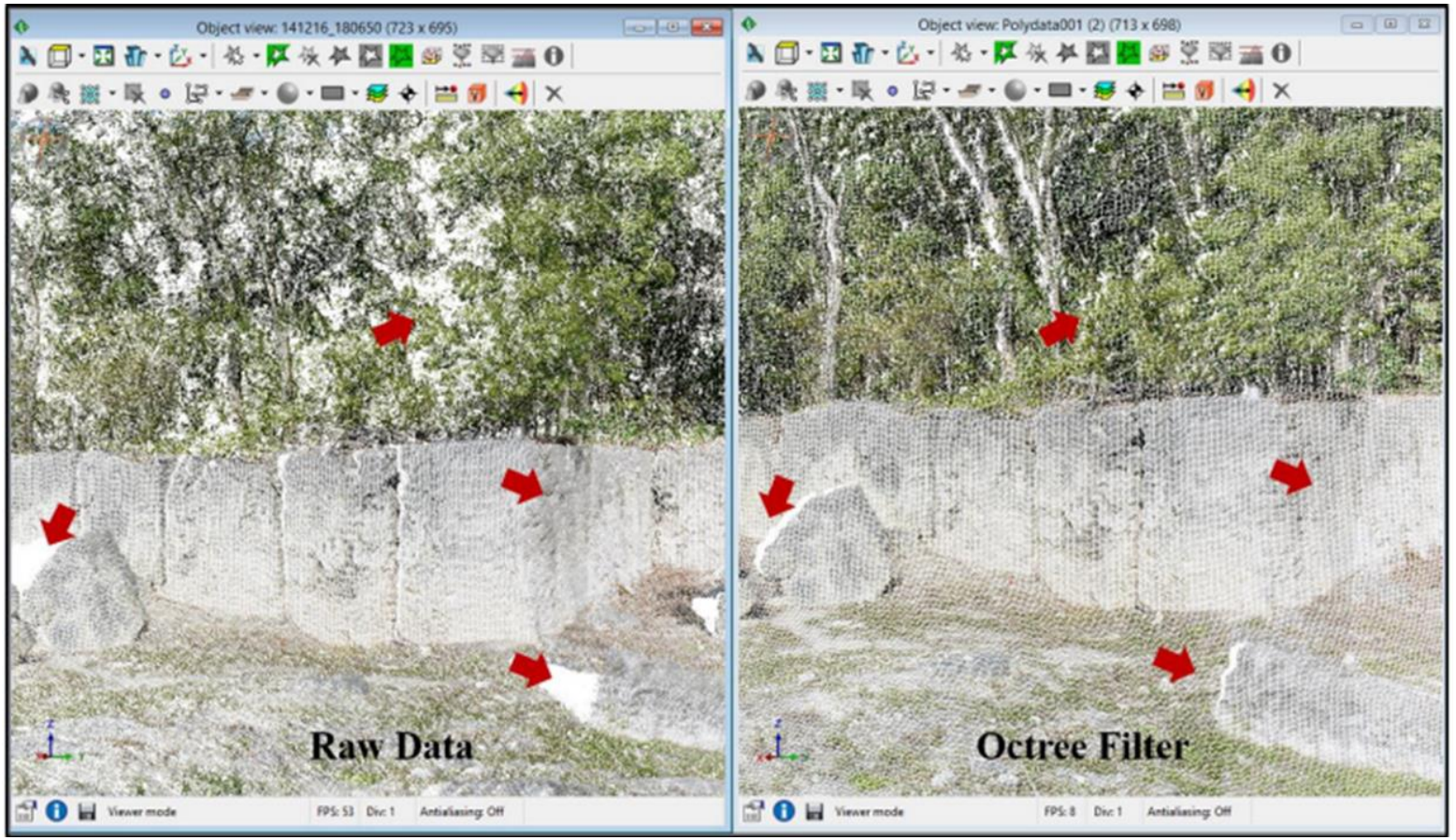

Figure 3.1 Showing colored raw scan data (left) and colored Octree-filtered data (right). Red areas indicate areas that Octree filter has significantly changed. (Giddens, 2016)

Split-FX

Data imported to the rock mass analysis software Split-FX are in XYZ ASCII format. The XYZ values represent the spatial dimension for each point where X is easting, Y is northing, and Z is elevation. When importing the colored scans to Split-FX, the user has the option to import a color spectrum for the data in RGB format where R is red, G is green, and B is blue. After the data are imported, point clouds are converted into a triangular mesh. The user has the option to choose the point density per triangle. I chose a 10-point spacing for each triangle. Triangulation can be used to reduce the impact of shadow zones by choosing larger point spacing for each triangle (Hanzel, 2014). After converting the point cloud data into a triangular mesh, patches are created by combining mesh triangles that are similar in dimension and orientation. Each patch represents a planar surface which can be any planar geologic feature such as a joint or a bedding plane. Because patches do not necessarily denote a fracture plane, the interpreter can adjust the patch creation parameters to allow Split-FX to accurately discriminate between planar geologic features. In creating the patches for this project, I defined each patch to be created based upon a minimum of six mesh triangles and 10° maximum angle between neighboring patches. The interpreter can later use the program to generate strike (± 180°) and dip data for each patch; hence each fracture plane. The user can also manually pick a fracture by creating polygons along fracture planes. Split-FX later measures strike and dip for the manually picked traces/fracture planes.

Chapter 4 Observation and Interpretations

General 3D of Canyon

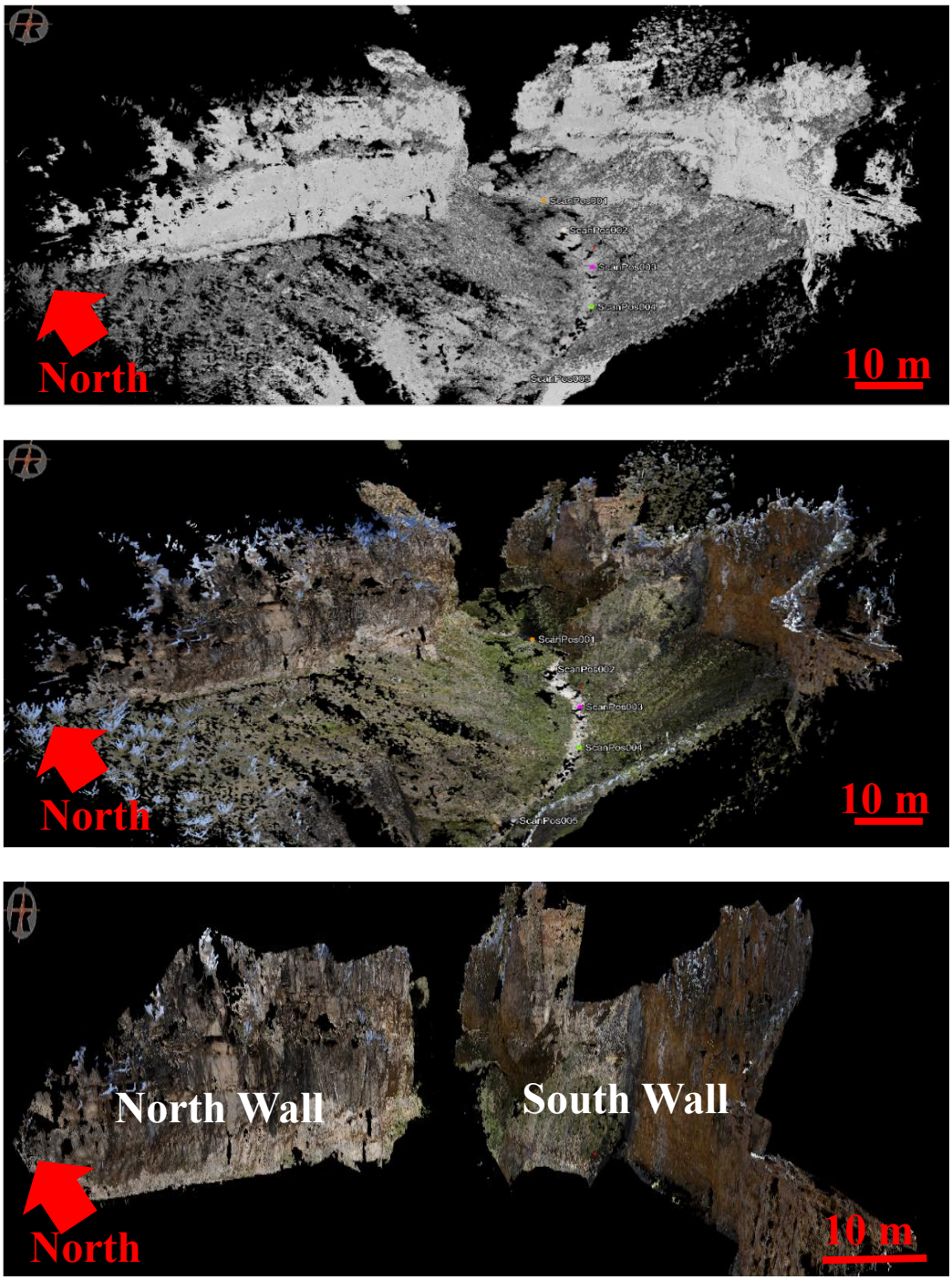

Figure 4.1. Showing the general morphology of the studied segment of the Bone Canyon. Top image showing raw LiDAR data. Middle image shows colored Lidar Data (unprocessed). Bottom image shows processed and colored LiDAR data.

Fracture Population

As a first order observation, the north and south walls of the Bone Spring formation with the Bone Canyon were subdivided into three discrete rock units: A, B, and C where A is the top unit, B is the middle unit, and C is the bottom unit, see Figure 4.2. Rock unit A is a thickly-bedded limestone. Rock Unit B is a silty dolomitic limestone. Rock unit C is a thinly-bedded silty/argillaceous limestone. The number of fracture planes that were automatically picked and analyzed on selected windows from the north and south walls were 4301, and 3148, respectively. Three major fracture sets were identified: E-W trending Fracture Set-1, N-S trending Fracture Set-2, and NE-SW trending Fracture Set-3. Fracture Set-1 was the most dominant fracture set and was present in both walls. The following section will discuss the lateral variations in fracture distribution for each rock unit within the north and south walls. In addition, fracture distribution within the same rock unit across the two walls will be compared.

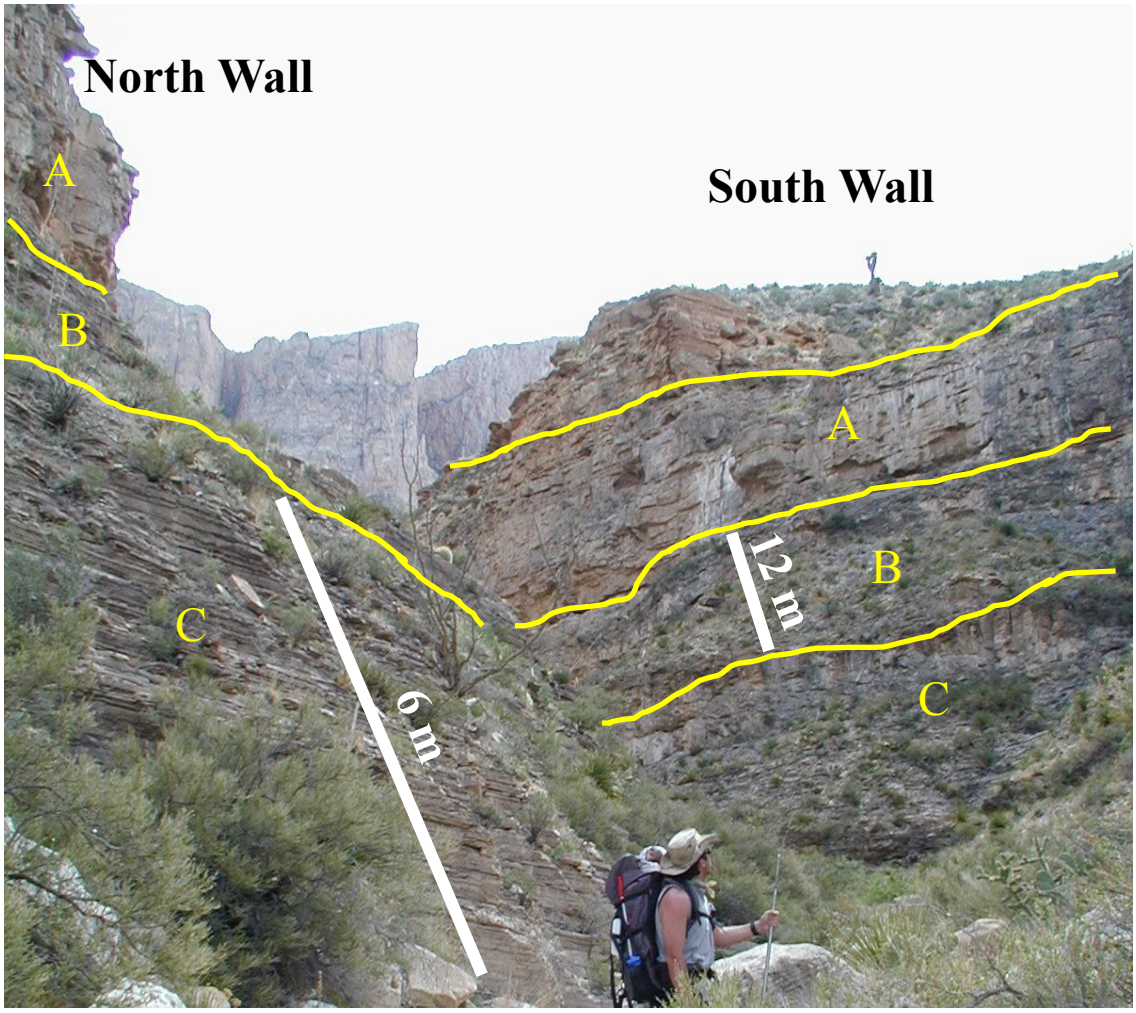

Figure 4.2 showing rock units: A, B, and C. Rock unit boundaries were based on field observation, termination of fractures, and LiDAR data. Modified after Elm Fork Natural Heritage Museum

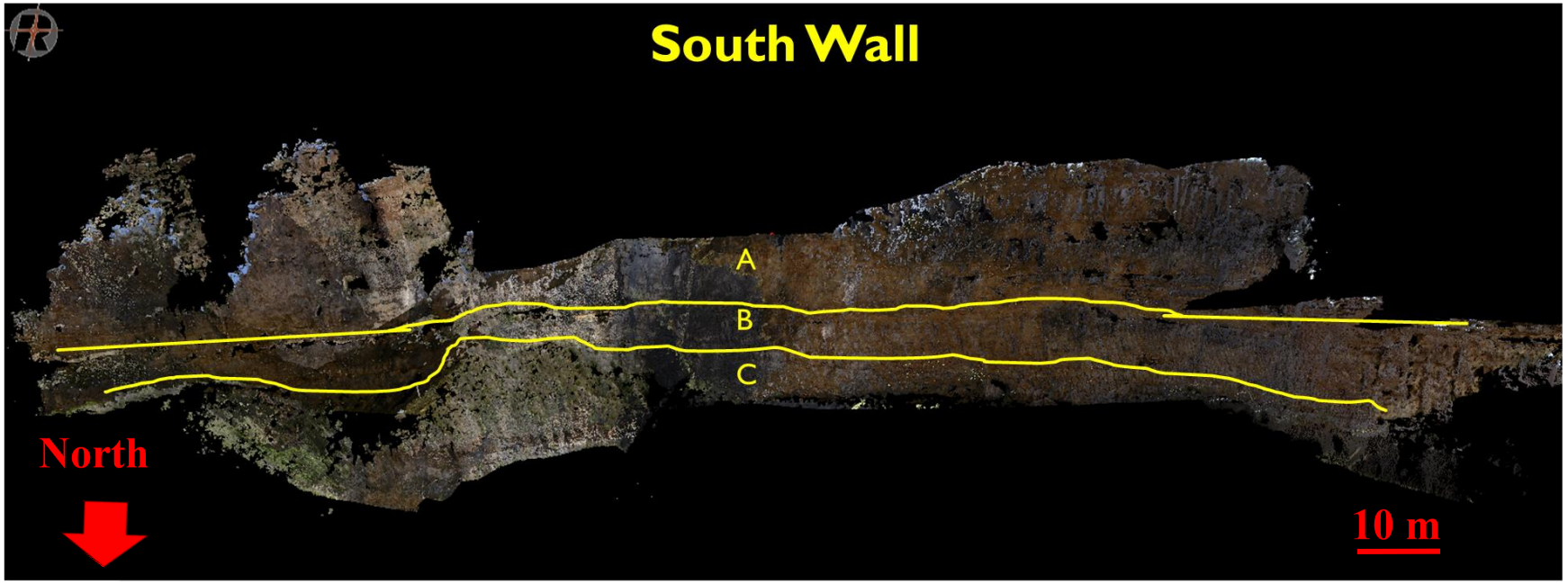

Figure 4.3 showing the subdivision of the south wall into three discrete rock units: A, B, and C (top to bottom). Subdivision was based on field observations, termination of fractures, and clear changes in lithology

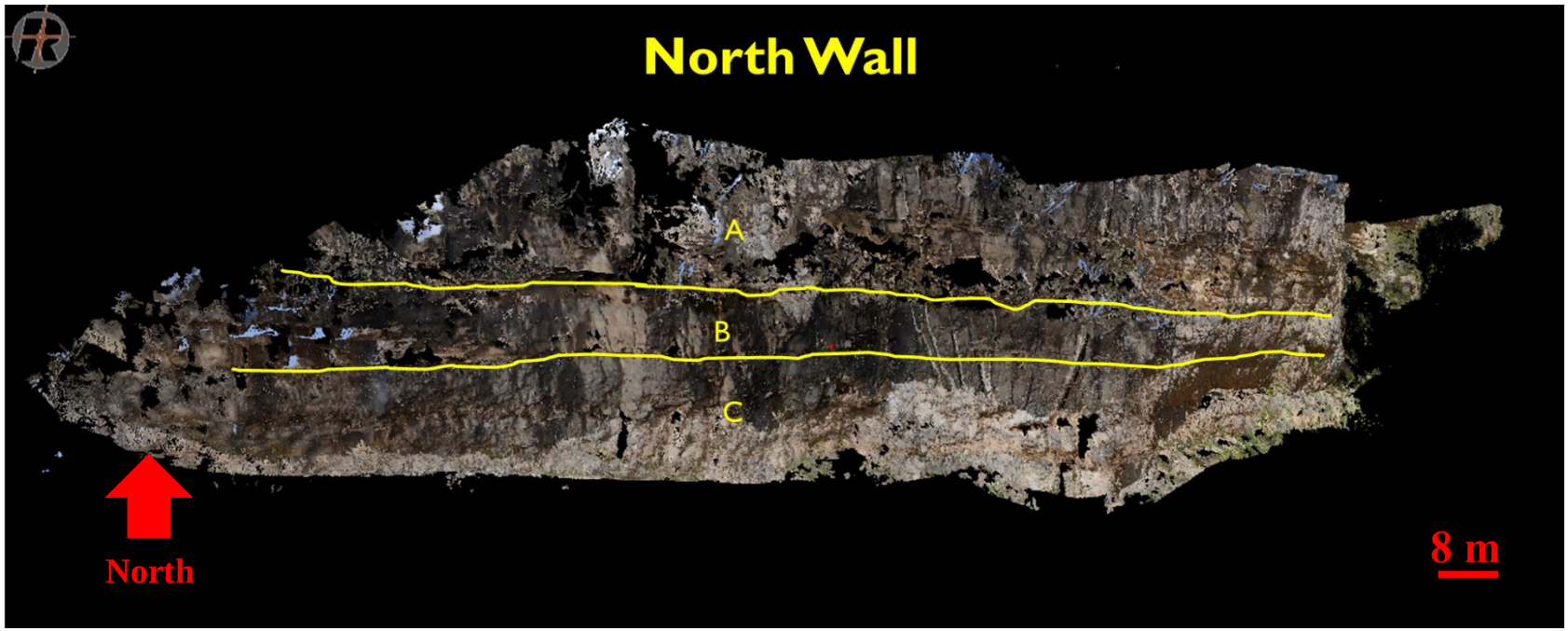

Figure 4.4 showing the subdivision of the south wall into three discrete rock units: A, B, and C (top to bottom). Subdivision was based on field observations, termination of fractures, and clear changes in lithology

South Wall: Rock Unit A

The face of this interpreted rock unit runs parallel to the general canyon direction (E-W). The face height ranges between 18-22 m while the length of this unit is around 100 m. The majority of fracture planes run 70-90° to the canyon wall in this rock unit. The chart below summarizes the fracture distribution of multiple windows representing Unit A along the southern canyon wall.

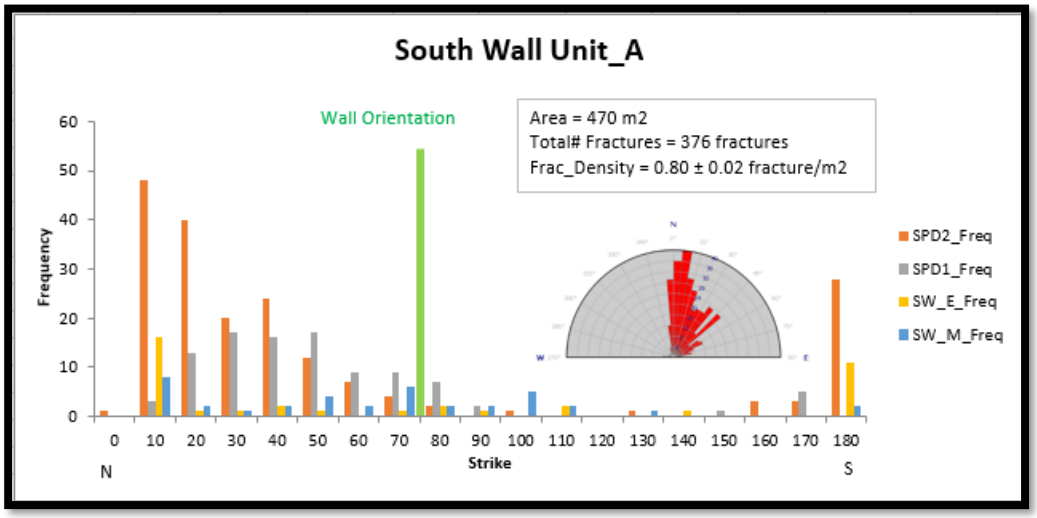

Figure 4.5 Fracture plane orientation distribution for Rock Unit A (South Wall), the legend indicates the names assigned to the interpreted point cloud data windows.

South Wall: Rock Unit B

The face of this rock unit runs parallel to the general canyon direction (E-W). The height ranges between 17-22 m while the length of this unit is around 100 m. The majority of fracture planes are 40-50° to the canyon wall in this rock unit. The chart

below summarizes the fracture distribution of multiple windows representing Unit B along the southern canyon wall.

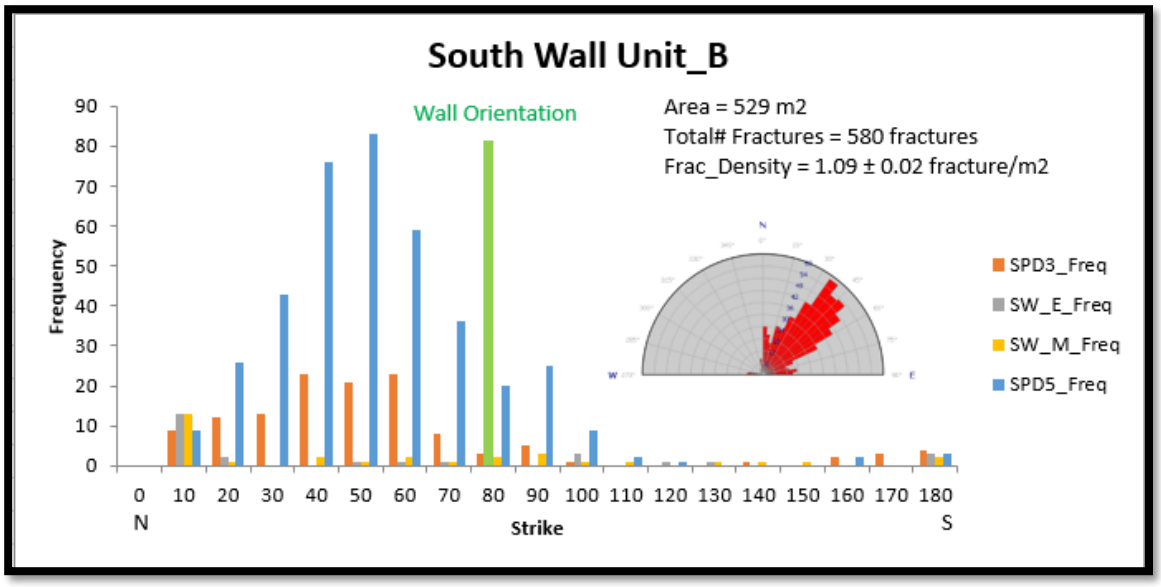

Figure 4.6 Fracture plane orientation distribution for Rock Unit B (South Wall), the legend indicates the names assigned to the interpreted point cloud data windows.

South Wall: Rock Unit C

The face of this rock unit makes a 10° intersection with the general canyon direction (E-W). The height ranges between 16-18 m while the length of this unit is around 100 m. The majority of fracture planes are 40-55° to the canyon wall in this rock unit. The chart below summarizes the fracture distribution of multiple windows representing Unit C along the southern canyon wall.

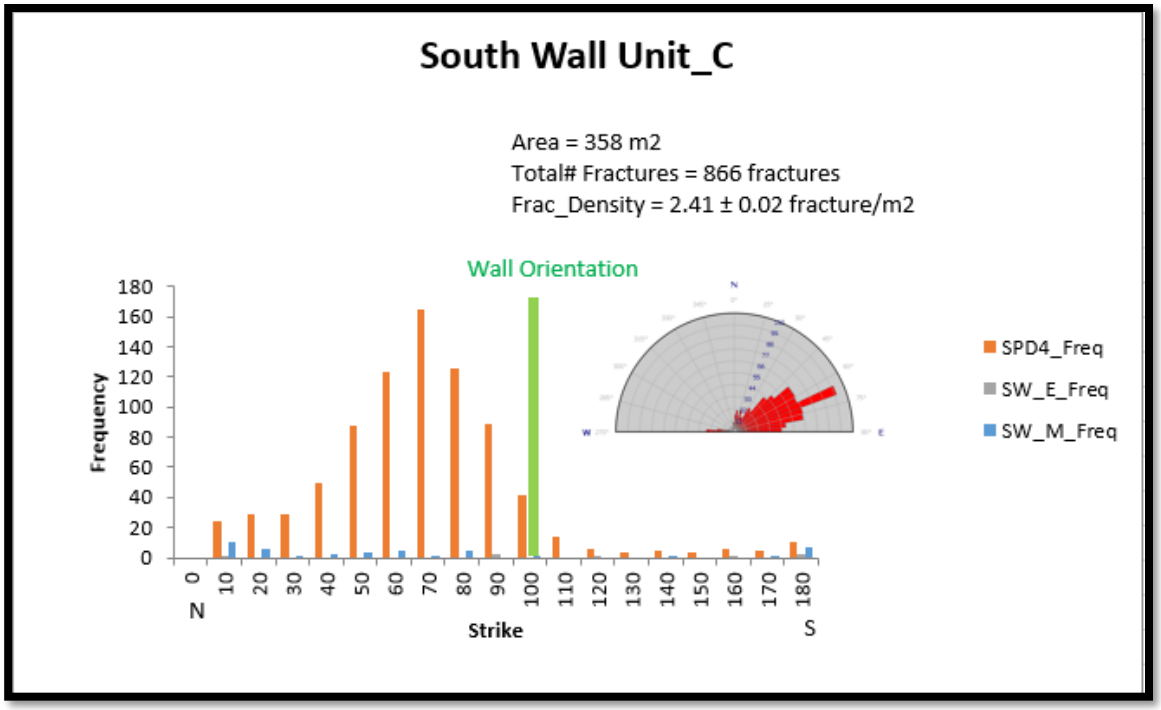

Figure 4.7 Fracture plane orientation distribution for Rock Unit C (South Wall), the legend indicates the names assigned to the interpreted point cloud data windows.

North Wall: Rock Unit A

The face of this rock unit makes a 10° intersection with the general canyon direction (E-W). The height ranges between 12-15 m the length of this unit is around 140 m. The majority of fracture planes are 10-30° to the canyon wall in this rock unit. Being almost parallel to the canyon/formation wall is indicative of lower confidence in the automatically picked fracture planes. Fractures that run parallel to the general trend of the canyon are more likely to be captured on east- and west-facing canyon walls but not the south- and north-facing walls. In this lithological unit along the north wall, there is a major set of fractures that makes 30-50° with the canyon wall. This set is indicative of higher confidence in the automatic picking compared to the aforementioned set. The chart below summarizes the fracture distribution of multiple windows representing Unit A along the northern canyon wall.

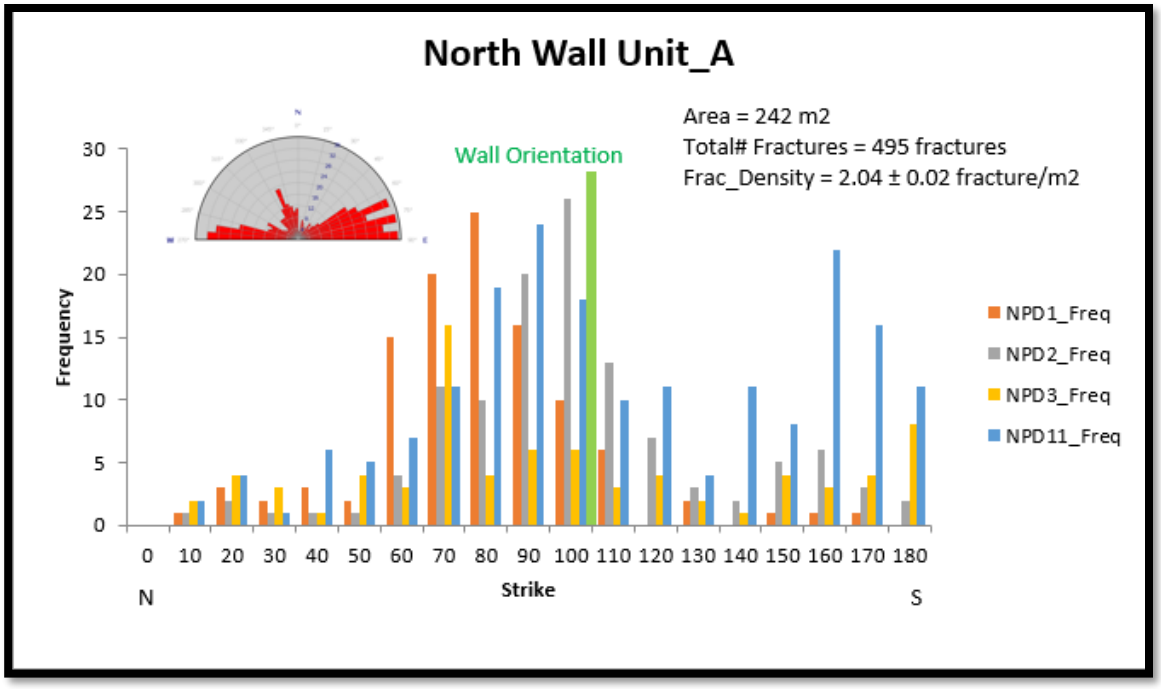

Figure 4.8 Fracture plane orientation distribution for Rock Unit A (North Wall), the legend indicates the names assigned to the interpreted point cloud data windows.

North Wall: Rock Unit B

The face of this lithological unit makes a five-degree intersection with the general canyon direction (E-W). The height ranges between 10-13 m while the length of this unit is around 140 m. The majority of fracture planes are 5-40° to the canyon wall in this rock unit. Being almost parallel to the canyon/formation wall is indicative of lower confidence in the automatically picked fracture planes. In this lithological unit along the north wall, there is a considerable number of fracture planes (around 30% of the total fracture population in this unit) that make 50-70°with the canyon wall. This set is indicative of higher confidence in the automatic picking compared to the aforementioned set. The chart below summarizes the fracture distribution of multiple windows representing Unit B along the northern canyon wall.

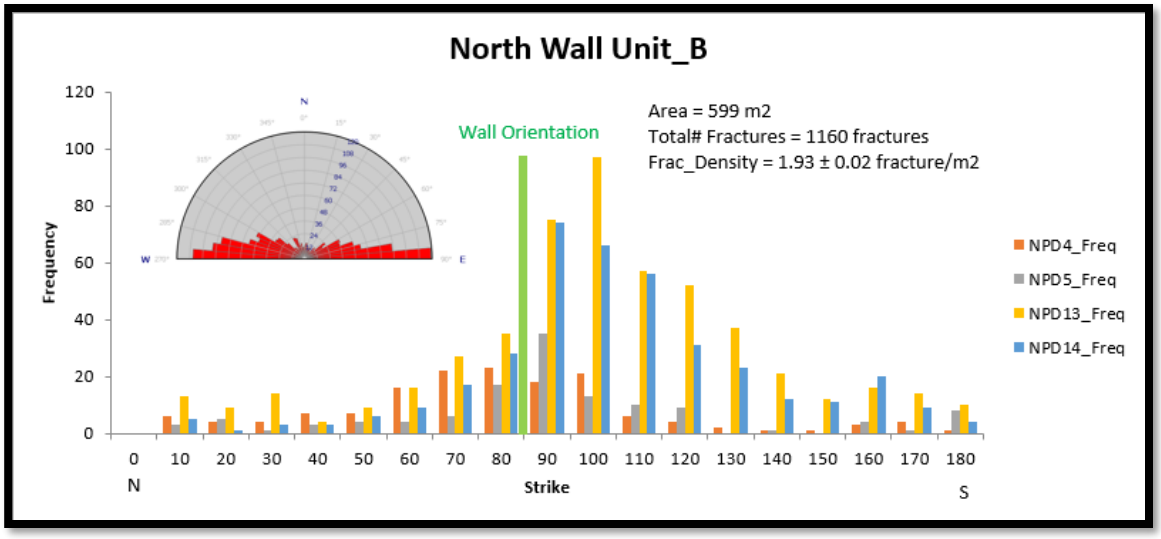

Figure 4.9 Fracture plane orientation distribution for Rock Unit B (North Wall), the legend indicates the names assigned to the interpreted point cloud data windows.

North Wall: Rock Unit C

The face of this rock unit makes a 15° intersection with the general canyon direction (E-W). The face height ranges between 10-13 m while the length of this unit is around 140 m. The majority of fracture planes are 5-40° to the canyon wall in this rock unit. Being almost parallel to the canyon/formation wall is indicative of lower confidence in the automatically picked fracture planes. In this lithological unit along the north wall, there is a considerable number of fracture planes (around 40% of the total fracture population in this unit) that make 50-90° with the canyon wall. This set is indicative of higher confidence in the automatic picking compared to the aforementioned set. The chart below summarizes the fracture distribution of multiple windows representing Unit C along the northern canyon wall.

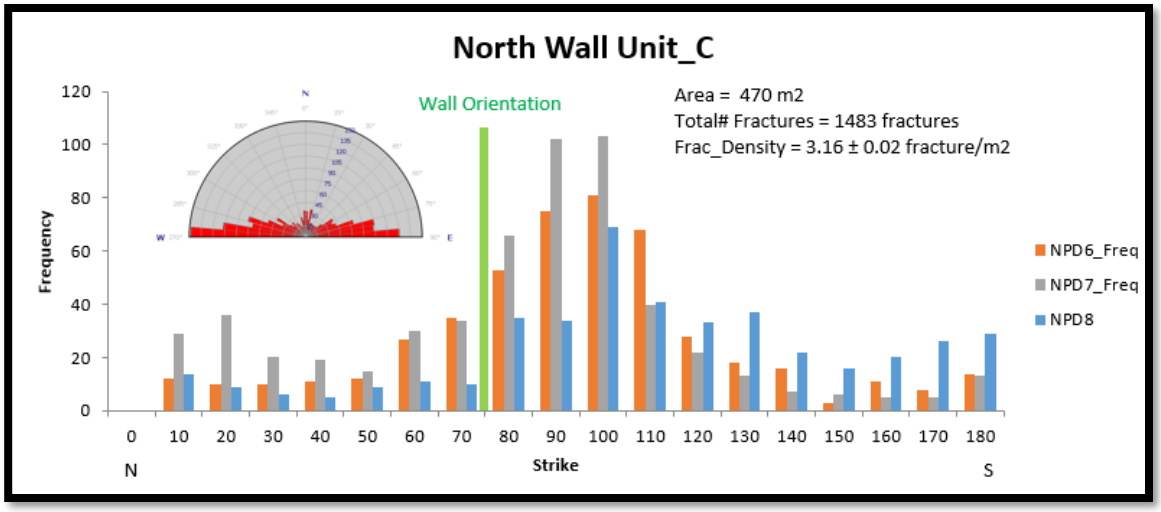

Figure 4.10 Fracture plane orientation distribution for Rock Unit C (North Wall), the legend indicates the names assigned to the interpreted point cloud data windows.

Lateral Fracture Distribution: Rock Unit-A, South Wall

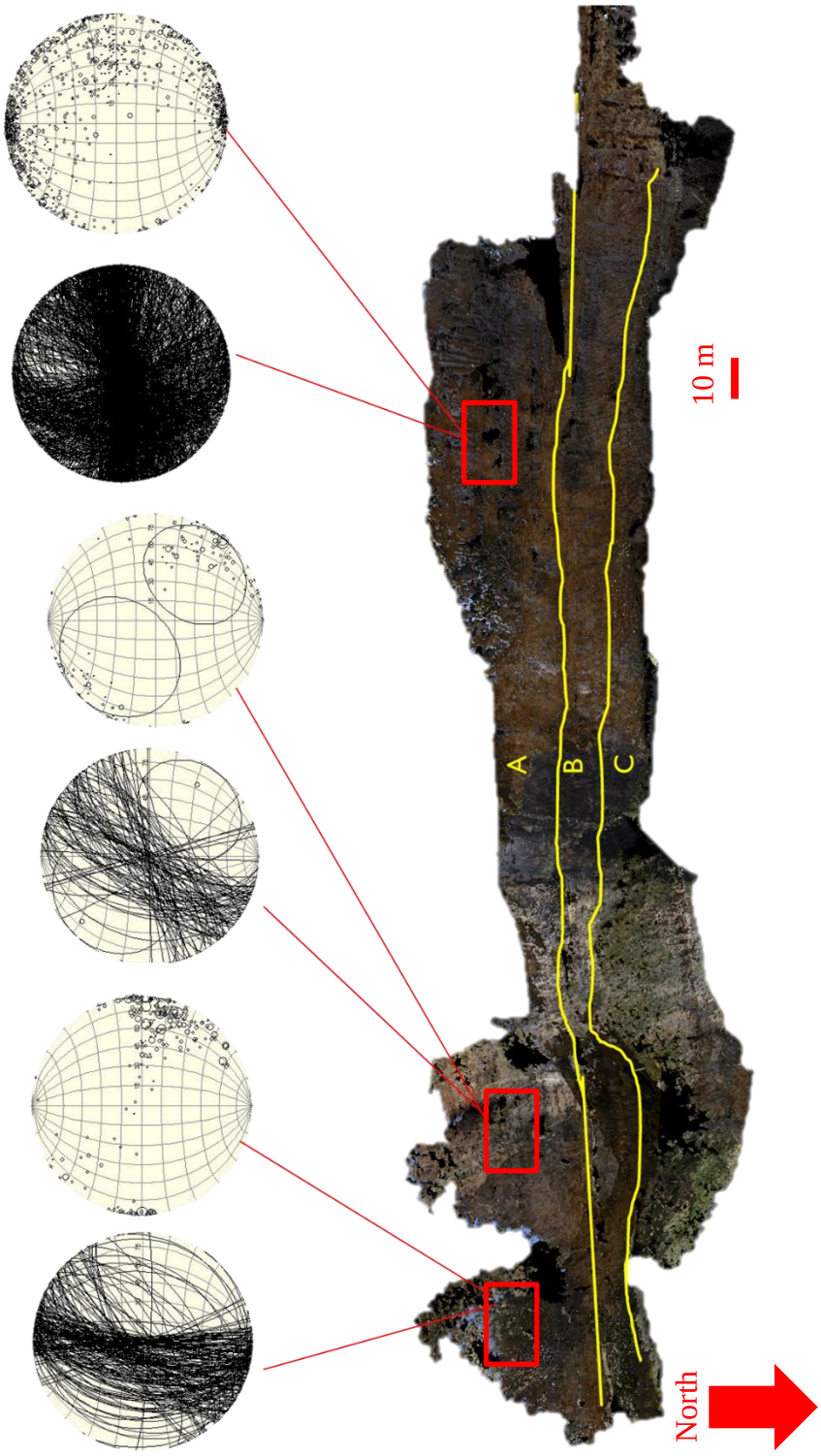

Figure 4.11 showing lateral distribution of fracture population in Rock Unit-A, South Wall. Major sets are trending E-W, N-S, and NE-SW. Redbox indicates the location and size of interpreted window

Lateral Fracture Distribution: Rock Unit-B, South Wall

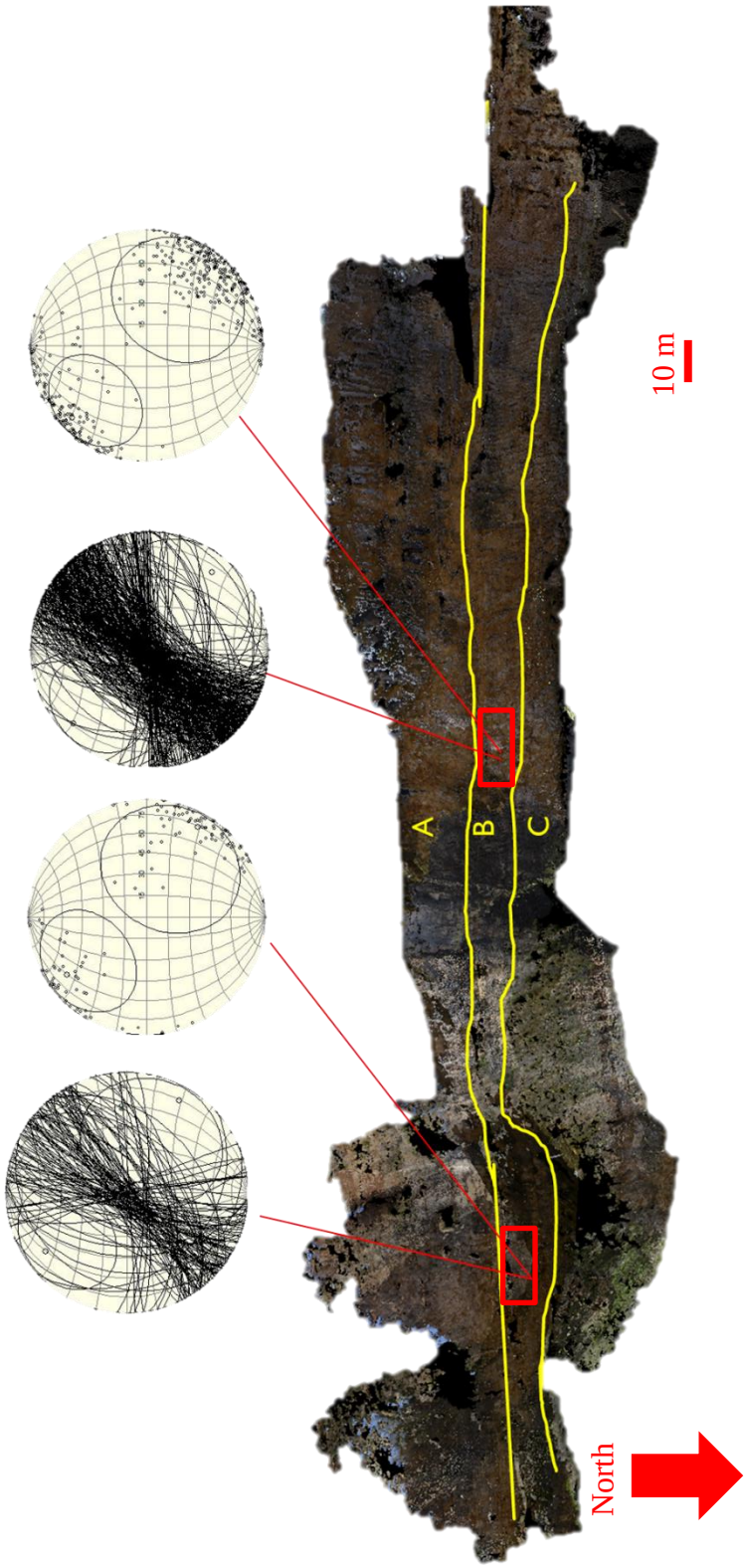

Figure 4.12 showing lateral distribution of fracture population in Rock Unit-B, South Wall. Major set is trending NE-SW. Redbox indicates the location and size of interpreted window

Lateral Fracture Distribution: Rock Unit-C, South Wall

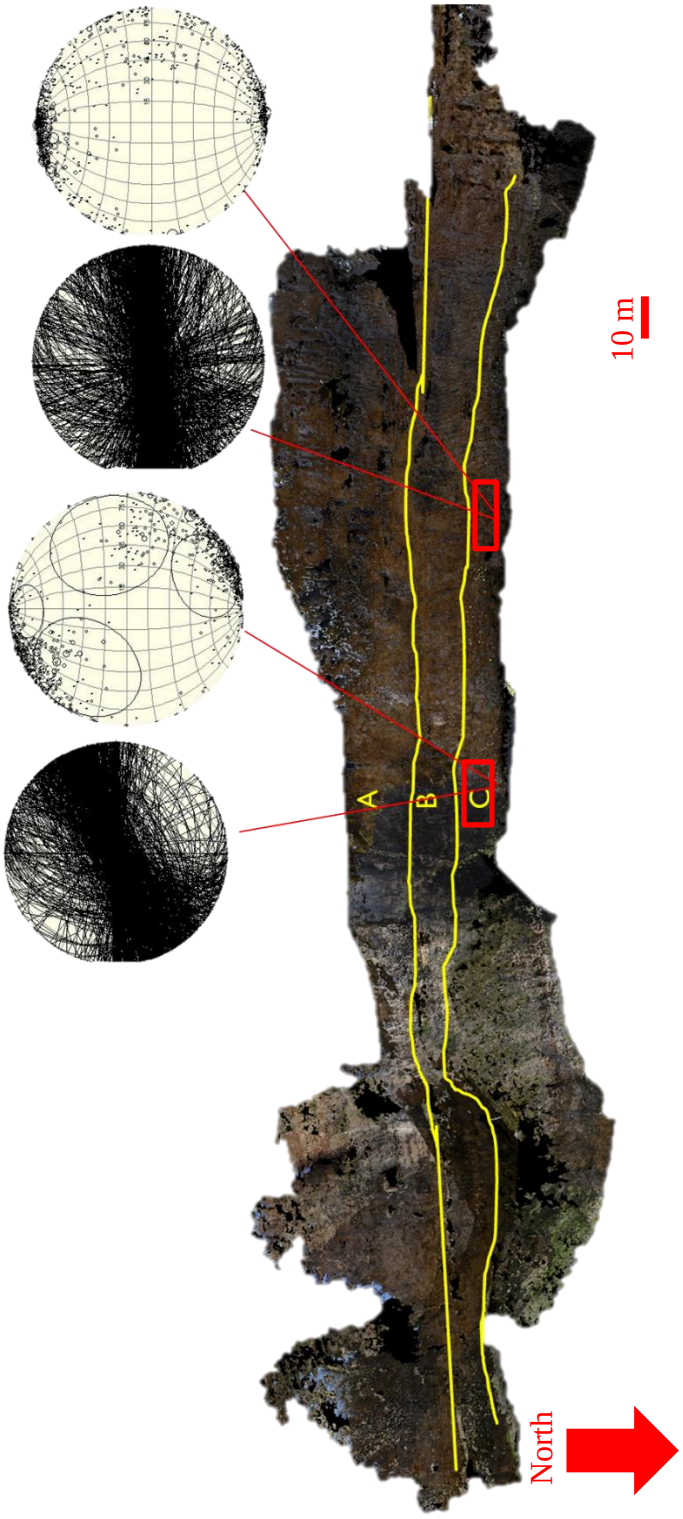

Figure 4.13 showing lateral distribution of fracture population in Rock Unit-C, South Wall. Major sets are trending E-W, and NE-SW. There is a subset that trends NW-SE. Redbox indicates the location and size of interpreted window

Lateral Fracture Distribution: Rock Unit-A, North Wall

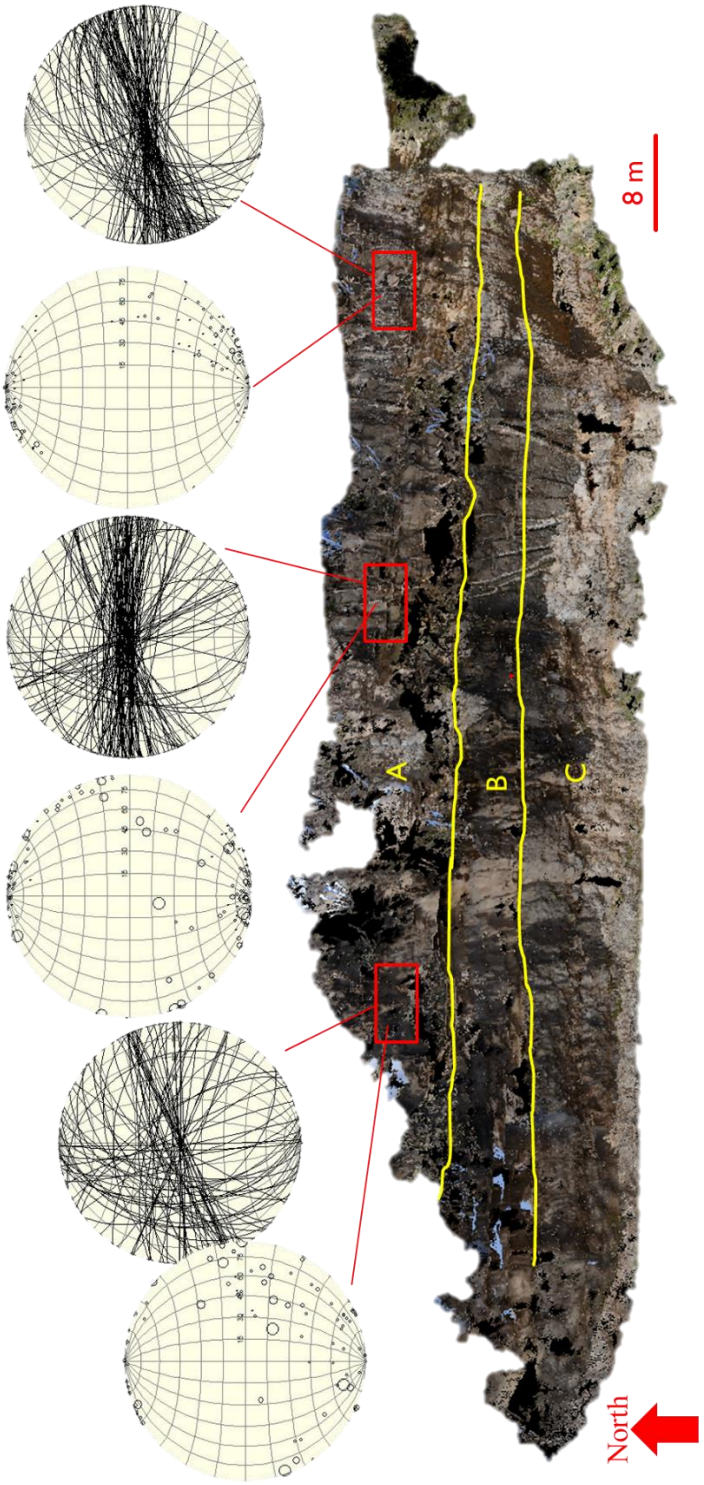

Figure 4.14 showing lateral distribution of fracture population in Rock Unit-A, North Wall. Major set is trending E-W. Redbox indicates the location and size of interpreted window

Lateral Fracture Distribution: Rock Unit-B, North Wall

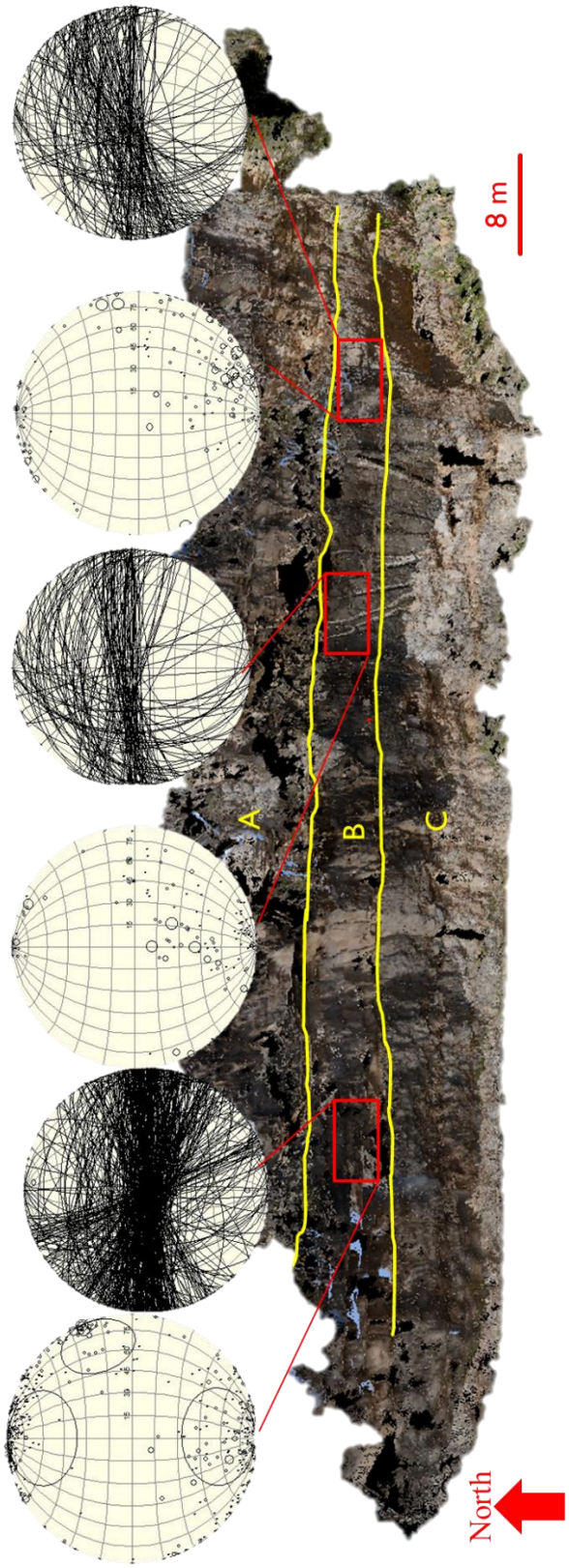

Figure 4.15 showing lateral distribution of fracture population in Rock Unit-B, North Wall. Major set is trending E-W. There is a subset that trends NW-SE. Redbox indicates the location and size of interpreted window

Lateral Fracture Distribution: Rock Unit-C, North Wall

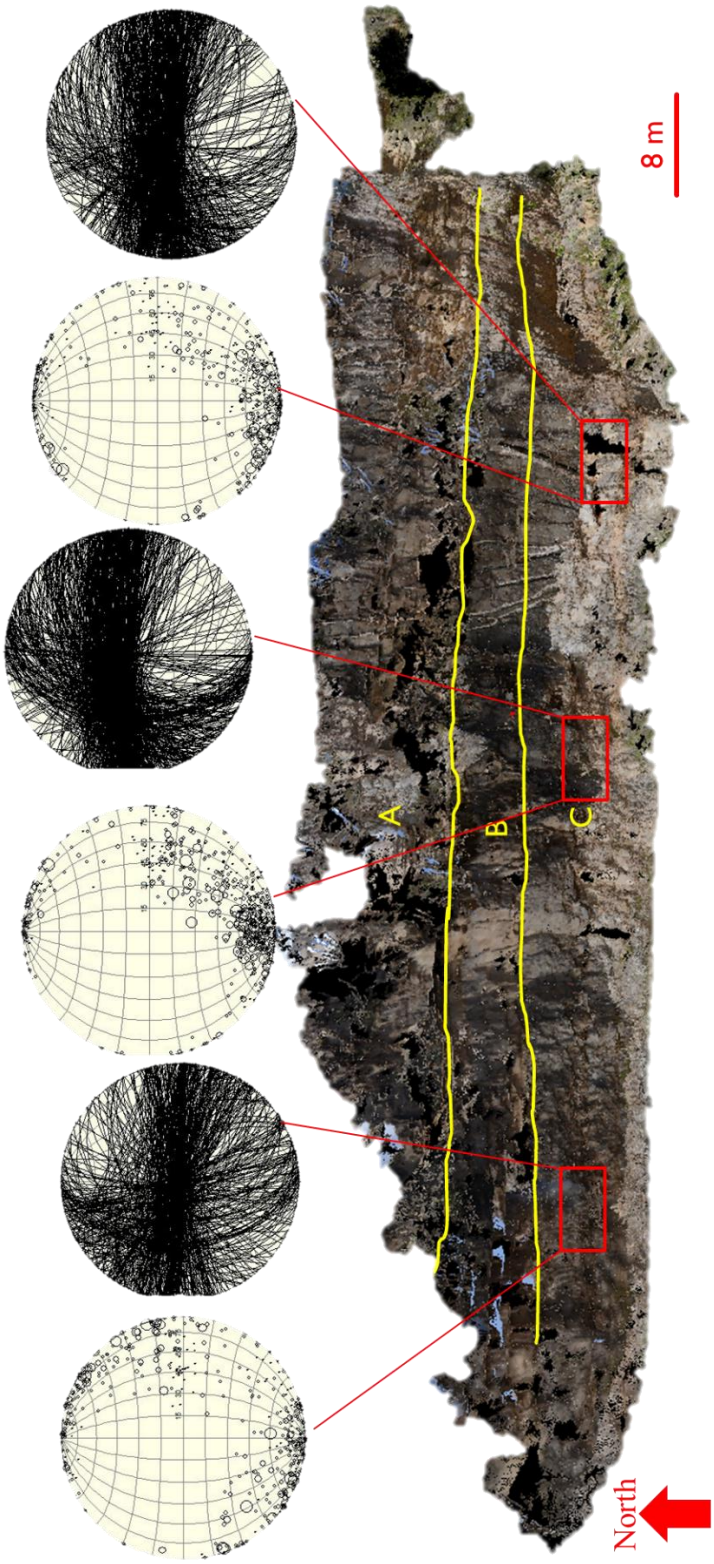

Figure 4.16 showing lateral distribution of fracture population in Rock Unit-B, North Wall. Major set is trending E-W. There is a subset that trends N-S. Redbox indicates the location and size of interpreted window

Comparing Fracture Populations Across the South and Walls

Fracture populations from each rock unit on the South Wall will be compared to fracture populations on the corresponding rock unit on the North Wall. Figure 4.17 provides a summary for all rock units within each wall

Rock Units A, B, and C: South and North walls (Summary)

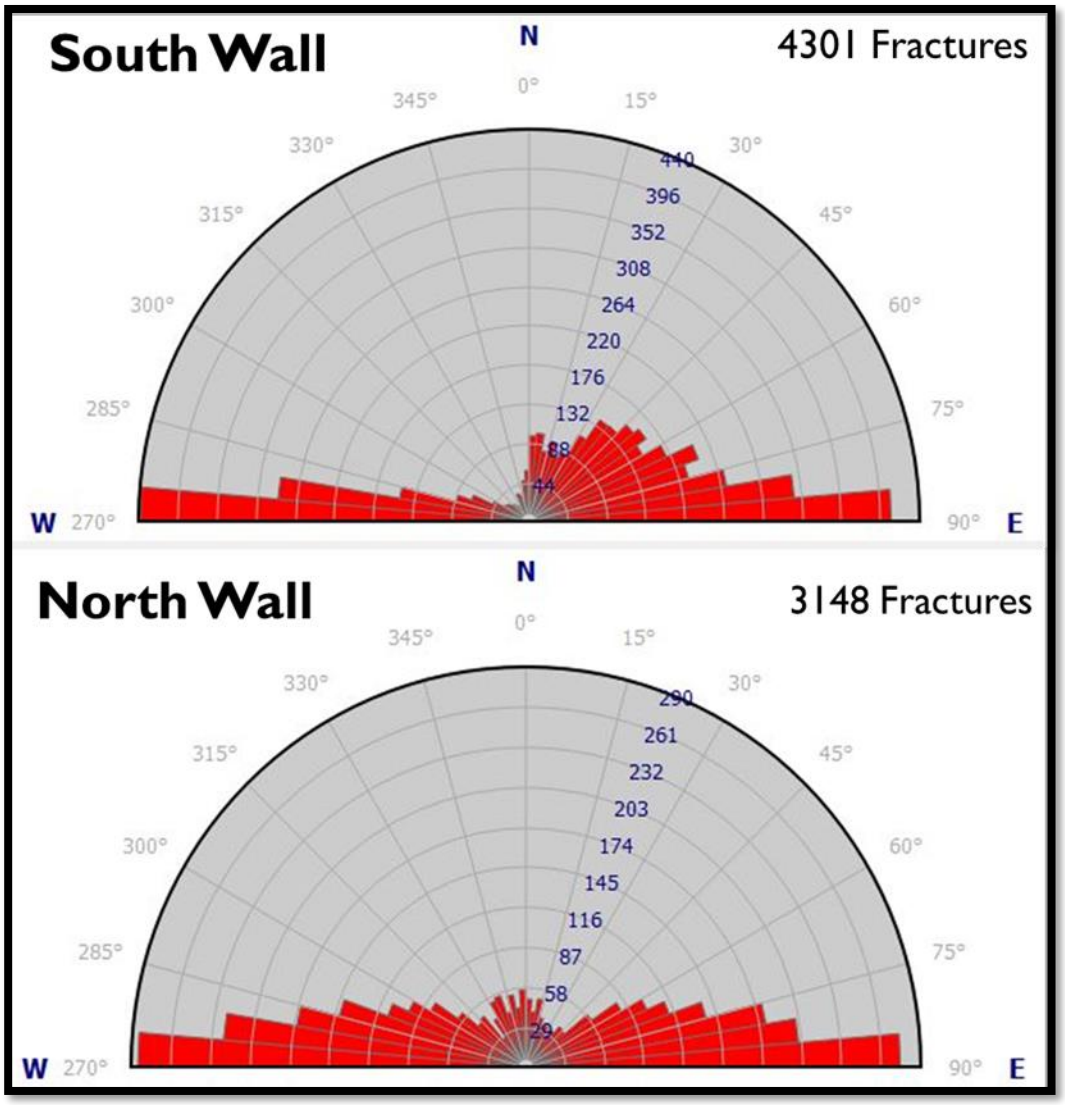

Figure 4.17 Comparison of fracture population from Rock Units A, B, and C in the South and North Walls. The major set is trending E-W. There are two other major sets trending N-S, and NE-SW

Rock Unit A: South and North walls

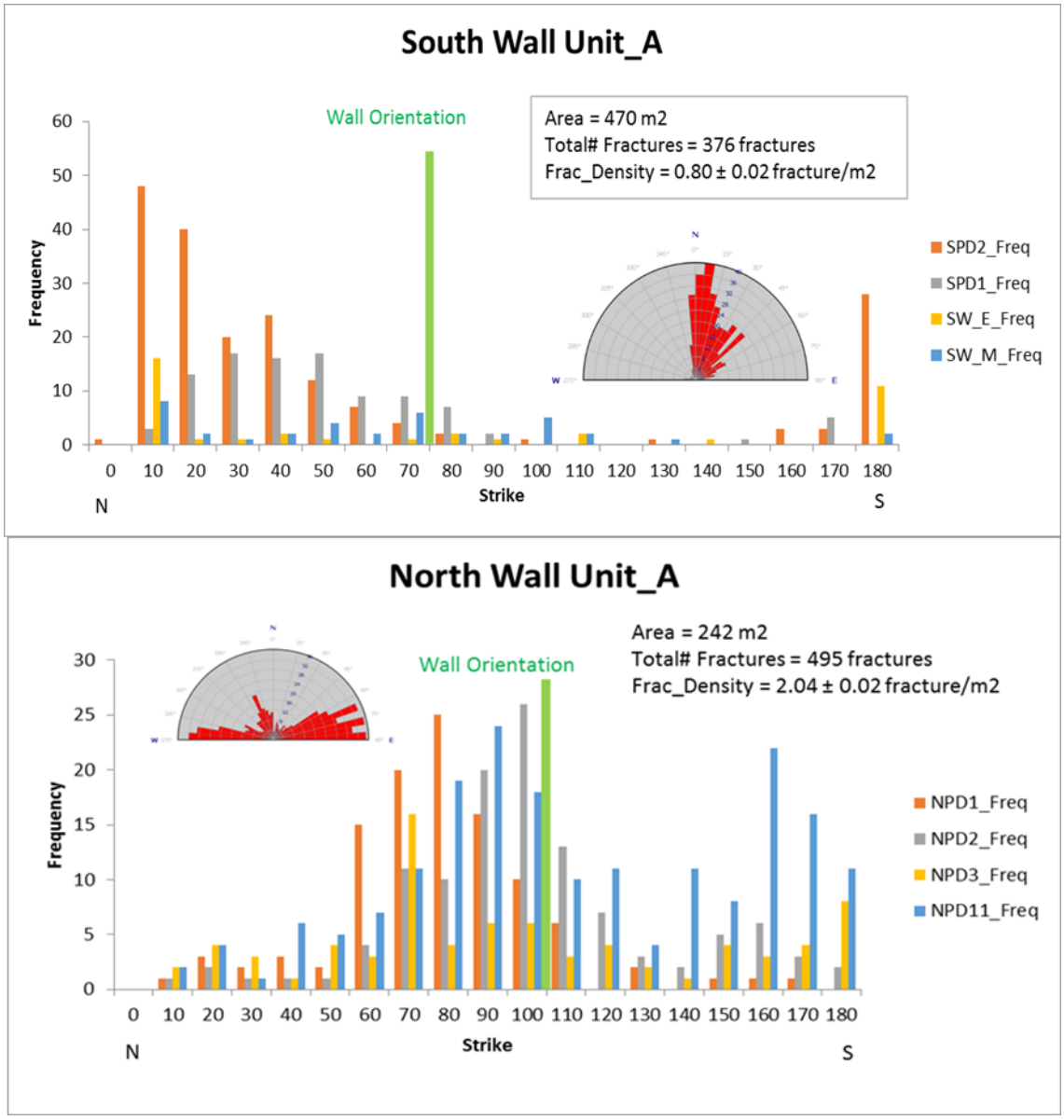

Figure 4.18 Rock Unit-A on the North Wall has higher fracture density than on the South Wall. Major fracture set in the North wall is trending E-W. Major fracture set in the South wall is trending N-S. The green bar indicates the strike of the canyon wall at the location of the interpretation window.

Rock Unit B: South and North Walls

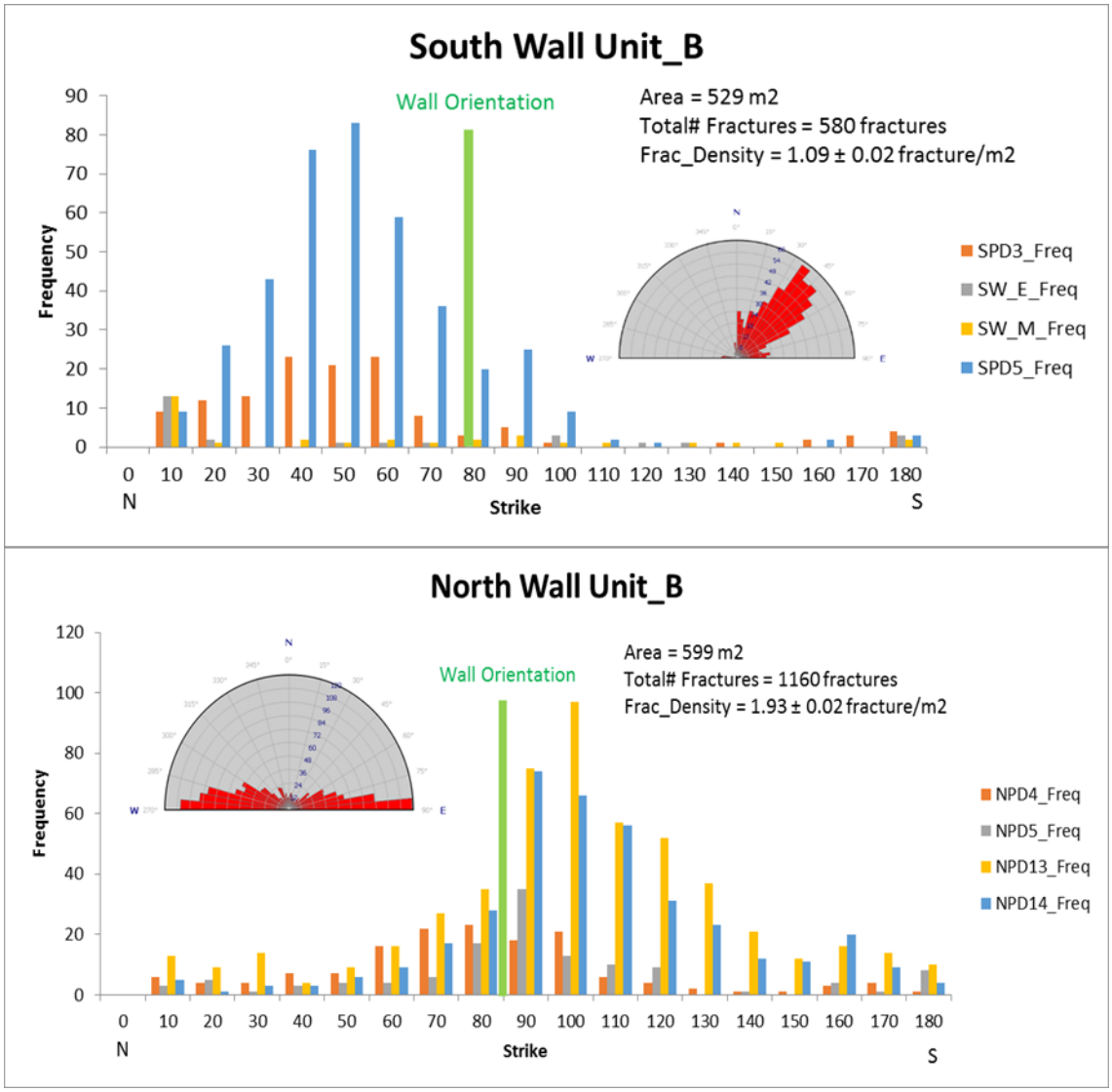

Figure 4.19 Rock Unit-A on the North Wall has higher fracture density than on the South Wall. Major fracture set in the North wall is trending E-W. Major fracture set in the South wall is trending NE-SW. The green bar indicates the strike of the canyon wall at the location of the interpretation window.

Rock Unit C: South and North walls

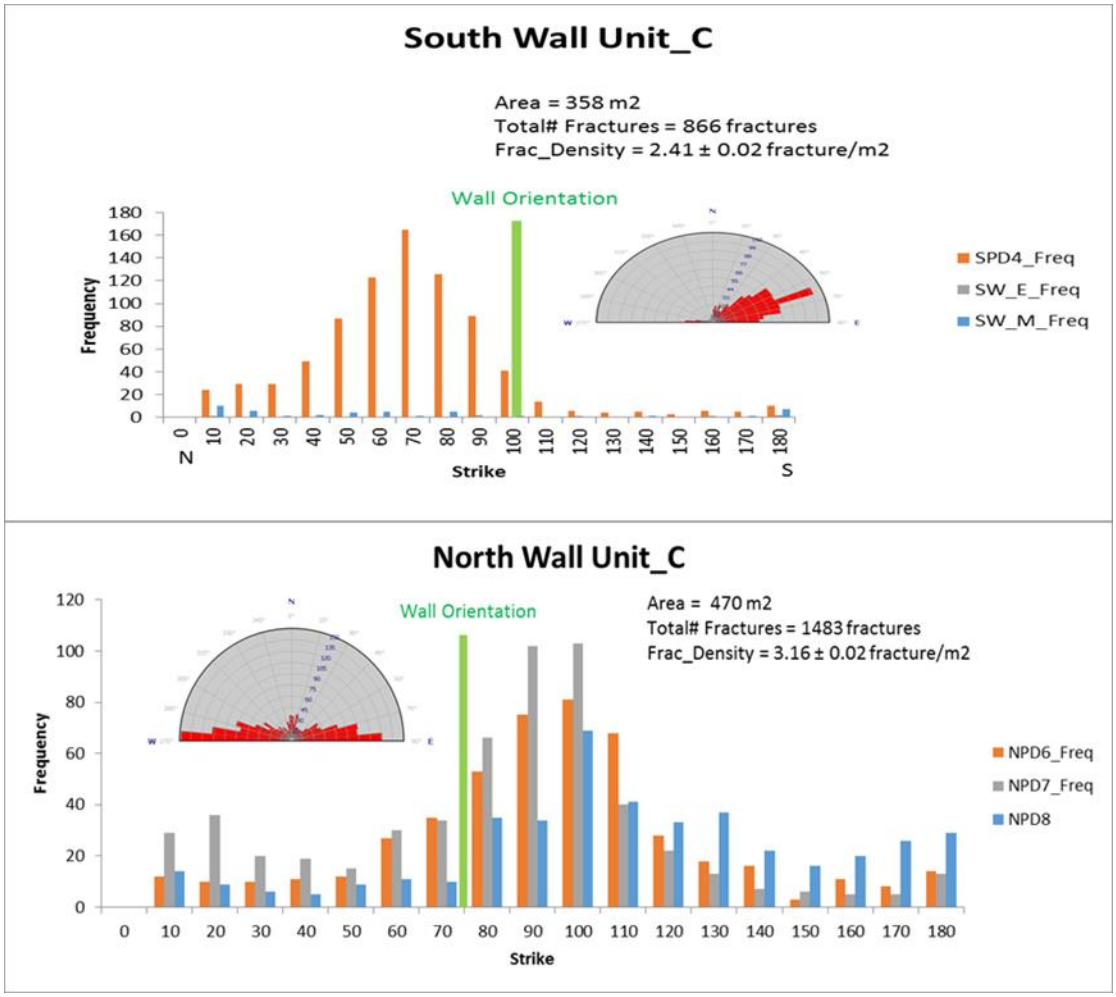

Figure 4.20 Rock Unit-A on the North Wall has higher fracture density than on the South Wall. Major fracture set in the North wall is trending E-W. Major fracture set in the South wall is trending NE-SW. The green bar indicates the strike of the canyon wall at the location of the interpretation window.

Addressing Bias in Fracture Distribution Between the South and North Walls

The possible reasons for bias observed in data can be a result of either/or a combination of the curvilinear nature of the canyon walls, stratigraphic variations between the two walls, and the locations of interpretation windows selected for fracture characterization. Canyon walls especially the south wall are curvilinear (see Figure 4.21) and this nature of the walls can affect the LiDAR efficiency in capturing fracture planes and as well the orientation of the populations present in the outcrop as fracture planes.

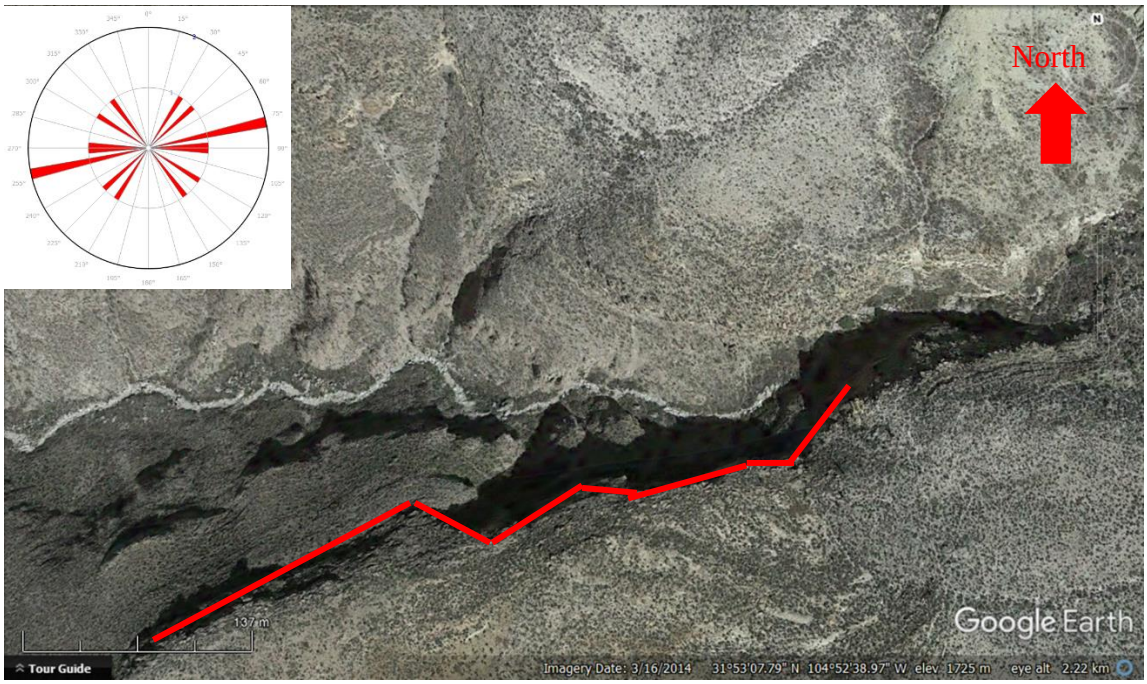

Figure 4.21 Showing the curvilinear nature of the south wall within the Bone Canyon.

Fractures planes perpendicular to the canyon wall will not delineated as a fracture plane; they will be delineated as a trace. In addition, fracture planes that run parallel to the Bone Canyon's general trend, that is E-W, will not be delineated as well because they do not intersect any wall with the same trend, see Figure 4.22.

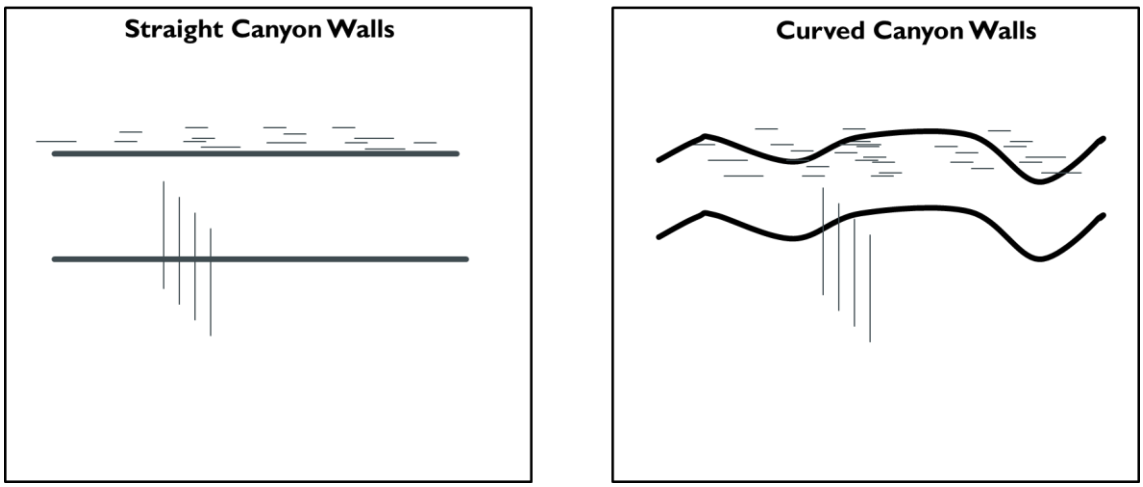

Figure 4.22 Showing the orientation of the canyon wall can affect whether a fracture appears on the outcrop as a plane or a trace. In addition, fractures that run parallel to canyon wall will not appear due to not intersecting with the canyon wall.

Stratigraphic Distribution of Fractures

This section focuses on the controlling factors for fracture distribution. Fracture density (number of fractures per square meter) within different sedimentary sequences was calculated and later used to find a correlation between stratigraphy and fracture distribution. Several stratigraphic units were defined and a characteristic relationship was found between unit thicknesses and fracture density; that is, fracture density increases if layer thickness decreases. This is observed in the interpreted section in this study when comparing fracture density data from the south wall (thicker units) and the north wall (thinner units). The north wall has an average fracture density of 2.6 fractures/m^2 while the south wall has an average fracture density of 1.23 fracture/m^2. As a qualitative observation, it was observed that fractures varied as well in their intensity (the degree of fracture propagation within a rock unit, measured in m/m and is found by subdividing fracture plane length over unit height). For different rock units, fractures varied between through-going to strata-bound (see Figure 4.23, and Figure 4.24). The majority of the through-going fractures were developed in the thicker units. The stratigraphic properties of the rocks control fracture intensity. Fracture intensity tends to increase with increasing brittleness (McGinnis et al, 2017). For example, layers with high abundance of limestone and quartz will most likely develop fracture systems with higher fracture intensity than layers with high abundance of clay minerals (McGinnis et al, 2017).

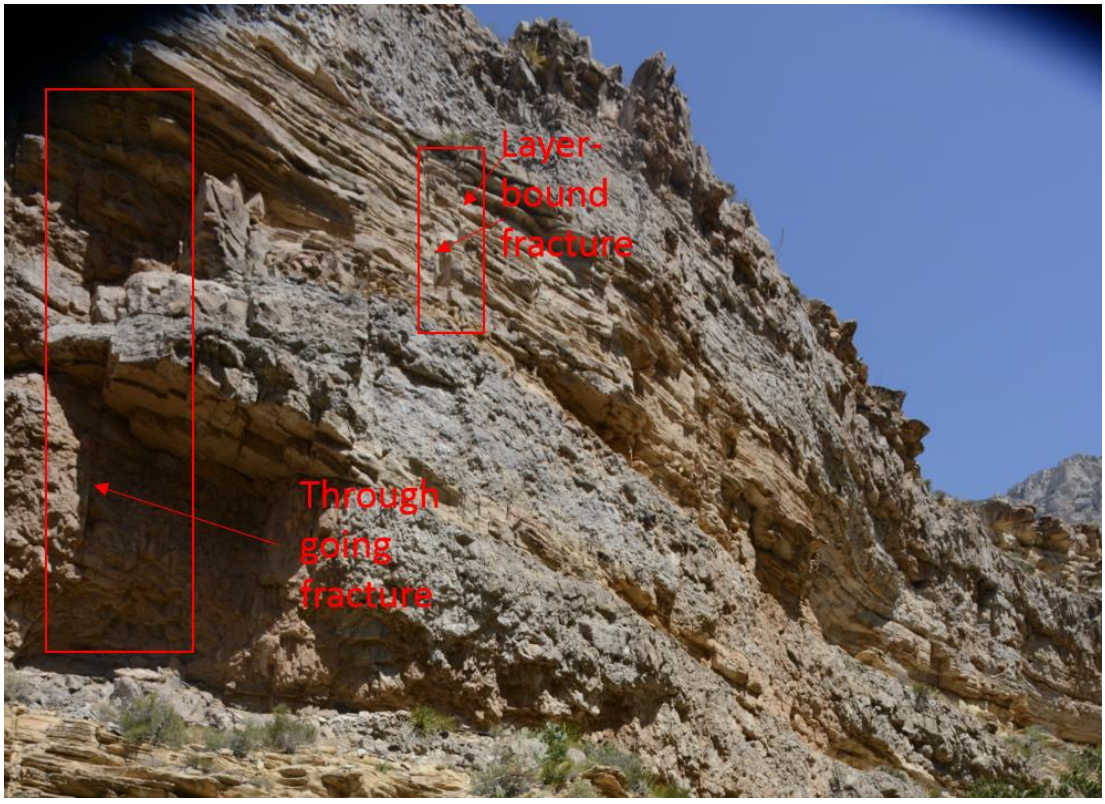

Figure 4.23 Examples of a through-going fracture (highlighted in red to the left) and a layer-bound fracture (highlighted red to the right).

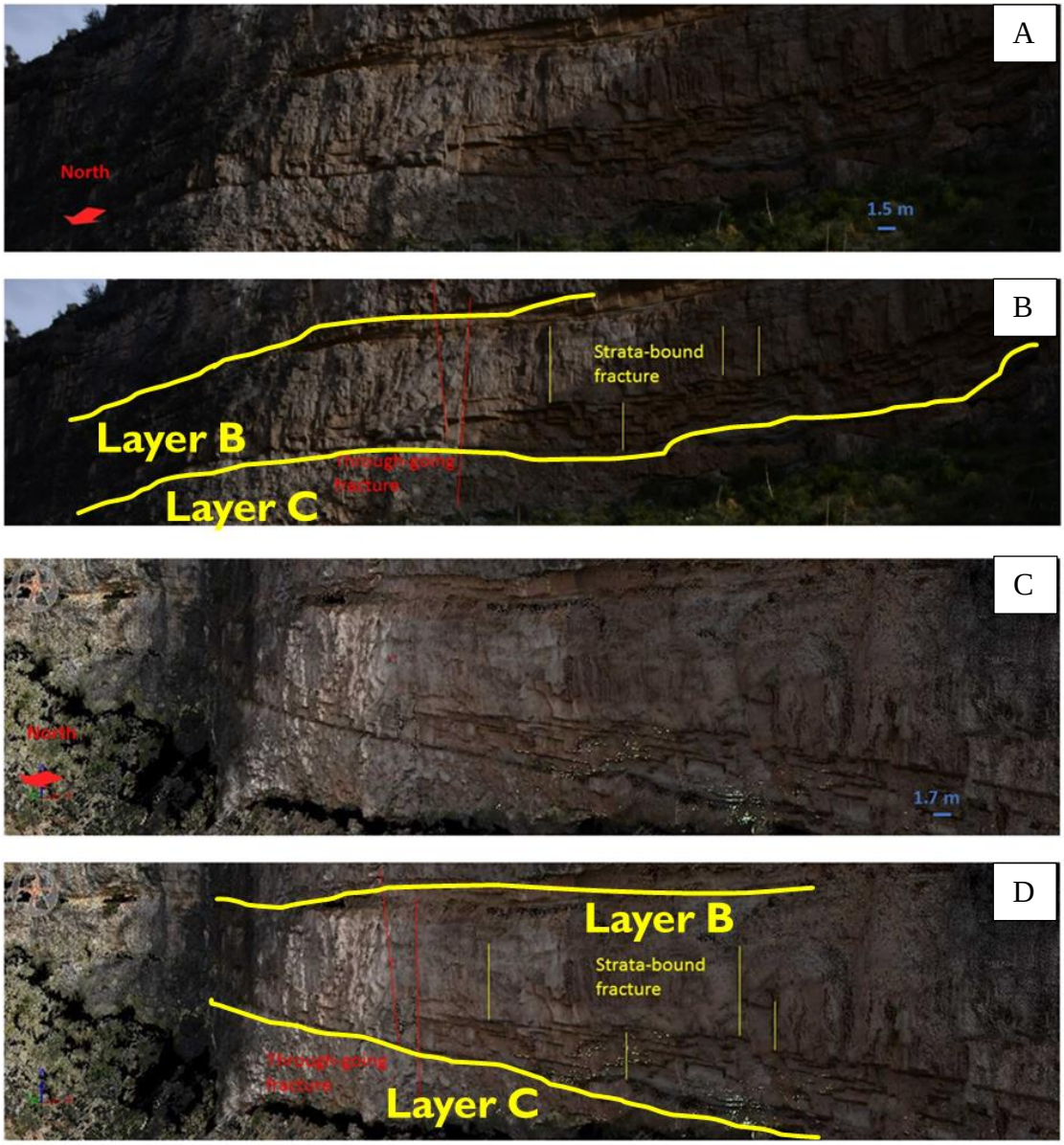

Figure 4.24 A, and B highlight strata bound and through-going fractures picked on photos captured using a Nikon D100. C, and D highlight the same strata-bound and through-going fractures picked on LiDAR data.

Trends in Fracture Plane Length Distribution

Fracture size is a major component for characterizing fractures. It controls the occurrence and size of rock masses, the behavior of shear planes, and the petrophysical properties of rock masses. A full characterization of fracture size is very difficult and requires thorough analysis of fracture surfaces in a three-dimensional environment. However, a good alternative for the three-dimensional analysis is to fracture planes in two dimensions (Li et al., 2014). Analyzing the fracture plane length (longest axis in a fracture plane) of a fracture system can serve as a good proxy for the three-dimensional fracture size distribution (Li et al., 2014). In this study, fracture planse were characterized by multiple windows that represent different lithological units. All the units displayed similar trends for fracture plane length distribution. In those lithological units, shorter fracture planes were more abundant than longer fracture planes; see Figure 4.25 for an example of fracture planes length distribution for Rock Unit-A in the North Wall. One issue that needs to be addressed is the sample size of the fracture plane data. Most of the software available on the market for characterizing fracture planes from Lidar data are not trained to automatically measure fracture plane length. This has a great impact on the accuracy of the fracture plane length distribution analysis. In this project, fracture plane lengths were manually measured from the Lidar acquired point cloud data.

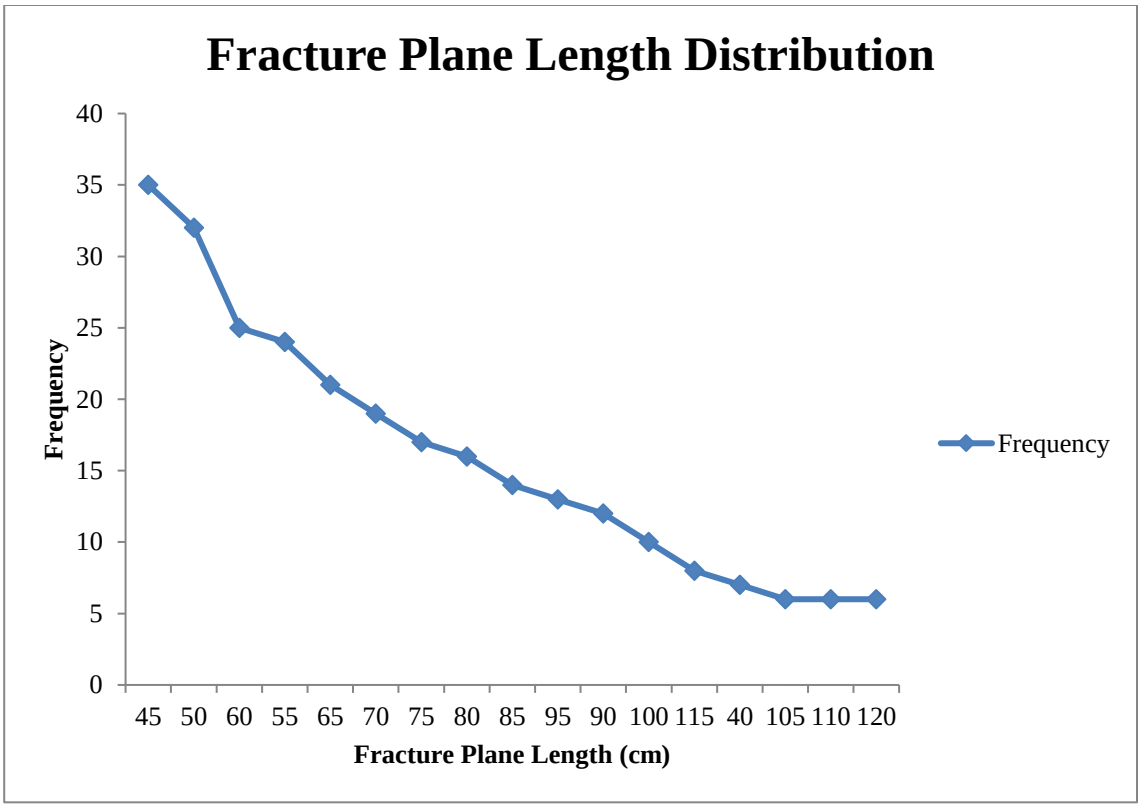

Figure 4.25 Distribution of fracture plane length that were sampled by multiple windows across North Wall's Rock Unit A.

Fracture Spacing

A total of six scanline surveys were conducted across the defined lithological units within the south and north canyon walls. Scanlines ran parallel to each wall and followed the changes in canyon geometry. All fractures that intersected a scanline were measured (strike, dip, length length). Through-going fractures were treated separately for each layer so if a through-going fracture intersected three lithologies, it was treated as separate fracture for each lithology. The general observation for fracture spacing is that it tends to increase with increasing thickness. A knowledge of the mean fracture spacing is important as it tends to influence the degree of fracturing within a mechanical unit (McGinnis et al, 2017).

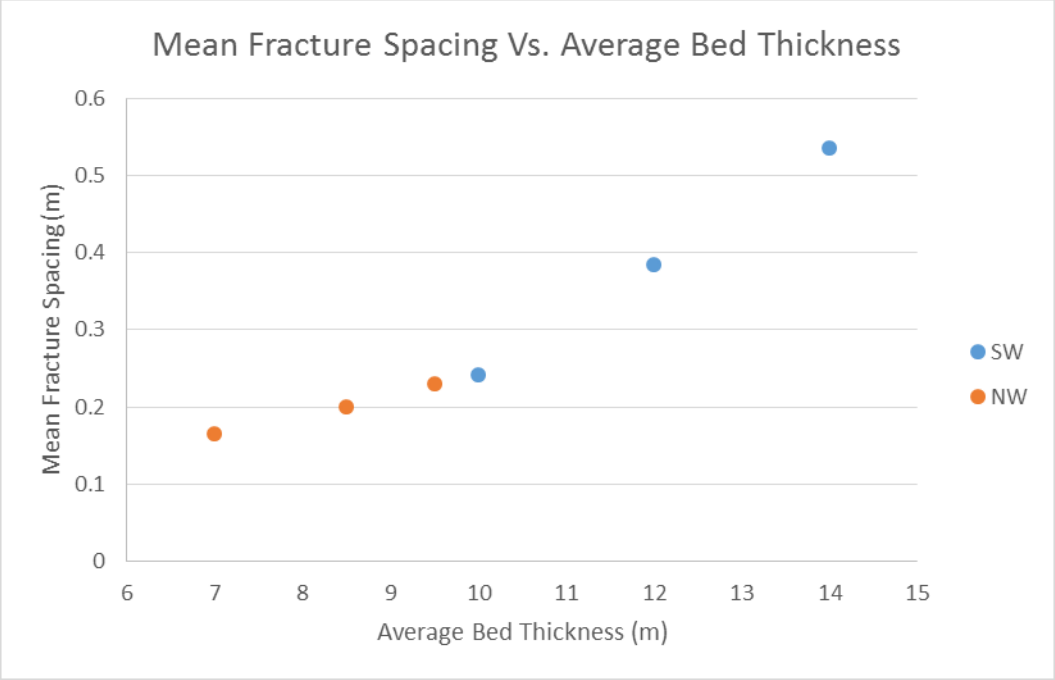

Figure 4.26 General trends in fracture spacing for different lithologies. Mean fracture spacing tends to increase with increasing bed thickness.

Chapter 5 Significance to Petroleum Exploration

The Bone Spring formation has been classified as an unconventional resource play (EIA, 2015). As in most unconventional plays, its reservoir potential is controlled by mineralogical distribution and the characteristics of the present fracture systems (Stolz, 2014). Unconventional reservoirs, in general, require stimulation through hydraulic fracturing. The process of hydraulic fracturing requires a good knowledge of the characteristics of the present fracture system in terms of its orientation, intensity, and density. This knowledge will serve as a predictive tool for how the hydraulic fractures are going to propagate and in selecting the proper zones for hydraulic fracturing (Stolz, 2014). This knowledge can help producers avoid drilling dry holes by understanding the nature of the fracture system and whether the present fracture systems are going to be conduits of water to the reservoir or not. The first horizontal Avalon shale attempt in 1991, by Strata Production, witnessed a "technical success" as gas was found in the matrix. However, fractures in the system were abundant and were conduits for water turning this technical success into a "financial dry hole." (Worrall & Krankawsky, 2011)

In general, natural fractures in unconventional resources are beneficial as they tend to create a network of flow pathways when a well is drilled and a treatment is pumped into the well. The presence of a natural fracture network containing some incipient fractures will aid the process of hydraulic fractures as those incipient fractures have the potential to be activated by hydraulic fracing. It must be kept in mind that hydraulic fractures orientation is controlled by the in-situ stress regime, while natural fractures orientations are the result of a paleostress regime.

Chapter 6 Conclusions

Studying the fracture system of the Bone Spring formation within the Bone Canyon was greatly facilitated by the utility of Light Detection and Ranging (LiDAR). The following points shed light on the essence of this study:

I. LiDAR technology is very useful in modeling fracture systems from outcrop data. It provides several advantages such as accessibility to regions where hand measurements are not possible, a greater density of data, and a convenient PC-powered platform for interpretation.

II. Fracture Set-1, Fracture Set-2, and Fracture Set-3 have been identified within the canyon trending to the following directions: E-W, N-S, and NE-SW, respectively. Fracture Set-1 is older and corresponds to a N-S sigma 3, Fracture Set-2 and Fracture Set-3 are younger an correspond to present day stress field that corresponds to a general E-W and NW-SE sigma 3, respectively.

III. The geometry of the canyon walls influences how the LiDAR measures fracture planes and must be accounted for. The general trend of the canyon was east-west. However, some parts of the south- and north-facing canyon walls were not perfectly trending east-west (5-40° off east-west). This allowed the LiDAR to capture the east-west trending fracture planes. However, the curvilinear nature of the canyon walls created some bias in the fracture distribution.

IV. Stratigraphy had an influence on fracture distribution; fracture density increased within thinner beds while fracture intensity increased within thicker beds.

V. All rock units displayed a similar trend for fracture plane length distribution. Fractures with shorter plane length were more abundant than fractures with longer plane length.

VI. Fractures varied between through-going to strata-bound. The majority of the through-going fractures were developed in the thicker units.

References

Adams, J. E., 1965, Stratigraphic-Tectonic Development of Delaware Basin: AAPG Bulletin, v. 49, p. 2140–2148, doi:10.1306/bc743de9-16be-11d7-8645000102c1865d.

Berman, A., 2016, Permian Basin Break-Even Price Is $61: The Best Of A Bad Lot: Forbes Magazine: <https://www.forbes.com/sites/arthurberman/2016/06/19/permian-basin-break-even-price-is-61-the-best-of-a-bad-lot/> (accessed May 3, 2017).

Crosby, C. B., 2015, Depositional history and high resolution sequence stratigraphy of the Leonardian Bone Spring Formation, Northern Delaware Basin, Eddy and Lea Counties, New Mexico: Norman, OK, University of Oklahoma.

Dutton, S. P., E. M. Kim, R. F. Broadhead, C. L. Breton, W. D. Raatz, S. C. Ruppel, and C. Kerans, 2016, Play Analysis and Digital Portfolio of Major Oil Reservoirs in the Permian Basin: Application and Transfer of Advanced Geological and Engineering Technologies for Incremental Production Opportunities: Bureau of Economic Geology at the University Of Texas at Austin and New Mexico Bureau of Geology and Minerals Resources at new Mexico Institute of Mining and Technology: <https://digital.library.unt.edu/ark:/67531/metadc888891/> (accessed May 3, 2017).

E. I. A., 2014, Six formations are responsible for surge in Permian Basin crude oil production - Today in Energy - U.S. Energy Information Administration (EIA): U.S. Energy Information Administration:

<https://www.eia.gov/todayinenergy/detail.php?id=17031> (accessed May 3, 2017).

E. I. A., 2016, U.S. Crude Oil and Natural Gas Proved Reserves, Year-end 2015: Energy Information Adminstration: <https://www.eia.gov/naturalgas/crudeoilreserves/> (accessed May 3, 2017).

Elm Fork Natural Heritage Museum, Guadalupe Mountains Graphic Resources: <http://efnhmuseum.unt.edu/graphic_resources/> (accessed May 12, 2017).

Gawloski, T. F., 1987, Nature, Distribution, and Petroleum Potential of Bone Spring Detrital Sediments Along the Northwest Shelf of the Delaware Basin: Society of Economic Paleontologists and Mineralogists, v. 87-27, p. 85–105.

Geologic Formations, n.d.: U.S. Department of the Interior: <https://www.nps.gov/cave/learn/nature/geologicformations.htm> (accessed May 3, 2017).

Giddens, E. L., 2016, Pleistocene coral reef destruction in the Florida Keys: paleotempestite evidence from a high resolution LIDAR XRF analysis of Windley Key Quarry, FL, Master's thesis, University of Oklahoma, Norman, Oklahoma, 189 p.

Hanzel, J. E., 2014, Lidar-based fracture characterization: an outcrop-scale study of the Woodford Shale, McAlister Shale Pit, Oklahoma, Master's thesis, Oklahoma State University, Stillwater, Oklahoma, 72 p.

Hart, B. S., 1997, New targets in the Bone Spring formation, Permian Basin: Oil&Gas Journal: <http://www.ogj.com/articles/print/volume-95/issue-30/in-this-issue/exploration/new-targets-in-the-bone-spring-formation-permian-

basin.html> (accessed May 3, 2017).

Keller, R. G., J. M. Hart, and R. Djeddi, 1980, A regional geological and geophysical study of the Delaware Basin, New Mexico and West Texas: Guidebook - New Mexico Geological Society, no. 31, p. 105–111.

King, P. B., 1948, Geology Of The Southern Guadalupe Mountains, Texas: U. S. Geological Survey Professional Paper, p. 183.

Li, X., Y. Zuo, X. Zhuang, and H. Zhu, 2014, Estimation of fracture trace length distributions using probability weighted moments and L-moments: Engineering Geology, v. 168, p. 69–85, doi:10.1016/j.enggeo.2013.10.025.

McGinnis, R. N., D. A. Ferrill, A. P. Morris, K. J. Smart, and D. Lehrmann, 2017, Mechanical stratigraphic controls on natural fracture spacing and penetration: Journal of Structural Geology, v. 95, p. 160–170, doi:10.1016/j.jsg.2017.01.001.

Montgomery, S. L., 1997, Permian Bone Spring Formation: Sandstone Play in the Delaware Basin Part I-Slope: AAPG Bulletin, v. 81 (1997), doi:10.1306/522b4dc5-1727-11d7-8645000102c1865d.

Nibbelink, M., 2016, Production Decline Curve Analysis -- The Road Not Taken: Forbes Magazine: <https://www.forbes.com/sites/drillinginfo/2016/07/05/production-decline-curve-analysis-the-road-not-taken/> (accessed May 3, 2017).

Stolz, D., 2014, Reservoir Character of the Avalon Shale (Bone Spring Formation) of the Delaware Basin, West Texas and Southeast New Mexico: Effect of Carbonate-rich Sediment Gravity Flows, thesis: University of Kansas, p. 165.

Worral, J., and C. Krankawoski, 2011, Geology and Development of the Bone Spring Formation In Loving County and adjacent areas: Part 2 Avalon Shale: AAPG Search and Discovery.